

*Chapter 3***O₂ constraints from Paleoproterozoic detrital pyrite and uraninite**

Jena E. Johnson^a, Aya Gerpheidea^{a,b}, Michael P. Lamb^a, Woodward W. Fischer^a

^aDivision of Geological and Planetary Sciences, California Institute of Technology, Pasadena, CA 91125, USA. ^bDepartment of Geology, Occidental College, Los Angeles, CA 90041

Originally published in the Geological Society of America Bulletin, Volume 126, Issue no. 5-6, p. 813-830.

ABSTRACT

Redox-sensitive detrital grains such as pyrite and uraninite in sedimentary successions provide one of the most conspicuous geological clues to a different composition of the Archean and early Paleoproterozoic atmosphere. Today these minerals are rapidly chemically weathered within short transport distances. Prior to the rise of oxygen, low O₂ concentrations allowed for their survival in siliciclastic deposits with grain erosion tied only to physical transport processes. After the rise of oxygen, redox-sensitive detrital grains effectively vanish from the sedimentary record. To get a better understanding of the timing of this transition, we examined sandstones recorded in a scientific drill core from the South African 2.415 Ga Koegas Subgroup, a mixed siliciclastic and iron formation-bearing unit deposited on the western deltaic margin of the Kaapvaal Craton in early Paleoproterozoic time.

We observed detrital pyrite and uraninite grains throughout all investigated sandstone beds in the section, indicating that the rise of oxygen is younger than 2.415 Ga. To better understand how observations of detrital pyrite and uraninite in sedimentary rocks can quantitatively constrain Earth surface redox conditions, we constructed a model of grain erosion from chemical weathering and physical abrasion to place an upper limit on ancient environmental O₂ concentrations. Even conservative model calculations for deltaic depositional systems with sufficient transport distances (ca. hundreds of kilometers) show that redox-sensitive detrital grains are remarkably sensitive to environmental O₂ concentrations, and constrain the Archean and early Paleoproterozoic atmosphere to have $< 3.2 \cdot 10^{-5}$ atm of molecular O₂. These levels are lower than previously hypothesized for redox-sensitive detrital grains, but are consistent with estimates made from other redox proxy data, including the anomalous fractionation of sulfur isotopes. The binary loss of detrital pyrite and uraninite from the sedimentary record coincident with the rise of oxygen indicates that atmospheric O₂ concentrations rose substantially at this time and were never again sufficiently low (< 0.01 atm) to enable survival and preservation of these grains in short transport systems.

INTRODUCTION

As early as the 1950s, geologists observed striking differences between the composition of grains found in conglomerates and sandstones from early Precambrian (ca. 2.4 Ga to

>3.25 Ga) sedimentary successions compared to modern deposits: the ancient sedimentary rocks contained grains of pyrite and uraninite (and occasionally siderite) in addition to the quartz, feldspar, lithic fragments, and heavy mineral grains (such as zircon, garnet, and monazite) commonly found in sediments of all age. The paleoenvironmental significance of these grains lies in their preservation during weathering and sediment transport. Both pyrite and uraninite minerals are prone to rapid oxidative chemical weathering (Grandstaff, 1976; Williamson and Rimstidt, 1994), and thus their relative abundance and preservation in siliciclastic successions implies that the Earth surface environments of weathering and sediment transport once contained less molecular oxygen (O₂) than today (Grandstaff, 1980; Holland, 1984; Prasad and Roscoe, 1996; Rasmussen and Buick, 1999).

The preservation of redox-sensitive detrital grains are one of several basic and fundamental geologic observations, including the secular distribution of banded iron formations, red beds, and the behavior of iron in paleosols, that indicate there was significantly less oxygen on the early Earth (Cloud, 1968, 1972; Holland, 1984). Redox-sensitive detrital grains have been documented in many studies, highlighting the global prevalence and magnitude of these deposits, albeit limited in time. To illustrate this secular distribution, we compiled a list of occurrences of redox-sensitive grains throughout the geologic record (Table 1). These grains are common in Archean strata, with the most recent occurrences documented in earliest Paleoproterozoic successions. It is likely that more occurrences exist waiting to be discovered, but a general pattern

emerges pointing to loss of redox-sensitive detrital grains from the sedimentary record sometime after 2.415 billion years ago (Johnson et al., 2013). Early Paleoproterozoic sedimentary deposits dated between 2.1 and 2.3 Ga (Kozhevnikov et al., 2010) appear to lack redox-sensitive detrital grains (the Jatulian Conglomerates; Clemmey and Badham, 1982). It is important to note that the presence of detrital pyrite and uraninite suggests the rise of atmospheric oxygen occurred sometime between 2.415 and ~2.1 Ga—timing consistent with the loss of multiple sulfur isotope anomalous fractionation and a range of other geological and geochemical proxies for oxygen, including the appearance of fluvial and nearshore marine red beds and gypsum deposits marking the onset of oxidative weathering in terrestrial environments (Roscoe, 1973; Cameron, 1982; Holland, 1984; Prasad and Roscoe, 1996; Rye and Holland, 1998; Tabakh et al., 1999; Beukes et al., 2002; Utsunomiya et al., 2003; Bekker et al., 2004; Papineau et al., 2007; Guo et al., 2009; Pufahl and Hiatt, 2012).

Compared to many other proposed proxies for O₂—which involve subtle and complex geochemical systems that remain poorly understood in both modern environments and geological materials—redox-sensitive detrital grains present a simple and straightforward redox proxy because they are easy to observe using light and electron microscopy and the mechanics behind the proxy are well understood. This notwithstanding, two broad challenges remain. 1) We still have a limited understanding of the secular distribution of these deposits (Table 1). Despite the relative ease of identifying these grains, many Archean and early Paleoproterozoic siliciclastic rocks have not been studied in detail for

the presence of redox sensitive detrital grains. Furthermore, few geochronological constraints, particularly in deposits surrounding the rise of O₂ (Hoffman, 2013), make it challenging to compare and contrast occurrences between basins with confidence. 2) While it is clear that lower O₂ concentrations are required to preserve redox-sensitive detrital grains through weathering and transport, the intertwined processes of chemical and physical weathering responsible for the destruction of these grains make it challenging to derive a quantitative constraint about environmental O₂ levels that allows for their preservation.

We recently reported detrital pyrite in a ~2.415 Ga sedimentary deposit from the western margin of the Kaapvaal Craton in South Africa (Johnson et al., 2013). Here we build on that report and address both of these challenges, beginning with a more detailed description and analysis of redox-sensitive detrital grains (including uraninite) throughout this early Paleoproterozoic deposit. Then, guided by these observations, but with broad applicability to all occurrences in the sedimentary record (Table 1), we describe the construction and results of a model combining a classic physical abrasion framework with previously determined chemical weathering rate laws to study grain erosion processes under different transport scenarios and environmental O₂ levels. This approach offers novel constraints and an upper limit on ancient oxygen concentrations for grain preservation across a range of different transport scenarios and depositional environments.

OBSERVATIONS FROM THE TRANSVAAL SUPERGROUP, SOUTH AFRICA

The South African Kaapvaal craton (Fig. 1A) harbors the first discovered and most well-known deposit with redox-sensitive detrital grains, the ~ 2.85 Ga Witwatersrand Supergroup placer deposits in the Central Rand Group (Liebenberg, 1955; Ramdohr, 1958), but also possesses several other key sedimentary successions of different ages that contain detrital pyrite and uraninite. The earlier ~ 3.08 Rhenosterspruit Formation bears detrital pyrite grains in a quartz-dominated conglomerate (Hiemstra, 1968; Simpson and Bowles, 1977; Hofmann et al., 2009), and the Mozaan Group has a granular quartz conglomerate at ~ 2.95 Ga with abundant pyrite pebbles (Hegner et al., 1994; Hofmann et al., 2009; Orberger et al., 2011). The ~ 2.7 Ga Ventersdorp Supergroup overlying the Witwatersrand is an unconformity-bound mixed volcanic and sedimentary succession with a basal unit of interbedded conglomerate and sandstone (Krapez, 1985). This unit has been well-characterized and has uraninite and pyrite grains in the sandy matrix of channel body conglomerates (Krapez, 1985). Heating and crustal thinning during Ventersdorp deposition created thermal subsidence, eventually allowing a marine platform to cover the craton (Schmitz and Bowring, 2003; Sumner and Beukes, 2006). Overlying the Ventersdorp is the Transvaal Supergroup, which begins with the Wolkberg Group in the eastern Transvaal basin and the Schmidtsdrif Subgroup in the western Griqualand West basin (Sumner and Beukes, 2006). The Wolkberg Group is unconformably overlain by the Black Reef Quartzite Formation, a thin conglomerate and quartzite unit with abundant pyrite and uraninite grains dated by basal correlation to ~ 2.64 but constrained by an ash bed 100 m above to slightly older than or ~ 2.59 Ga

(Walraven and Martini, 1995; Martin et al., 1998; England et al., 2002; Hofmann et al., 2009).

The Kaapvaal Craton was subsequently flooded by a shallow epicratonic sea, resulting in a long-lived carbonate platform (the Campbellrand-Malmani Platform, Fig. 2) originally deposited over the entire craton, an area $>600,000 \text{ km}^2$ (Beukes, 1987; Sumner and Beukes, 2006). At ~ 2.521 to 2.46 Ga , the carbonate platform gradually drowned and transitioned into deeper water deposition of iron formation, which is found in both the Transvaal basin (Penge Iron Formation) and Griqualand West (Kuruman Iron Formation) structural basins (Beukes, 1987; Simonson and Hassler, 1996; Sumner and Bowring, 1996; Sumner and Beukes, 2006). In the Griqualand basin, the Griquatown Iron Formation overlying the Kuruman records the filling of accommodation space on the western margin of the craton, from banded into shallower water granular iron formation (Beukes and Klein, 1992). The sequence continues to shoal into the $\sim 2.415 \text{ Ga}$ Koegas Subgroup which contains key intervals of siliciclastics. While the Black Reef Quartzite is the youngest unit underlying the Campbellrand-Malmani Platform to have facies appropriate for bearing redox-sensitive detrital grains, the Koegas Subgroup marks the first deposits overlying the carbonate platform with the appropriate lithologies to examine for redox-sensitive detrital grains (Fig. 2).

The Koegas Subgroup from Griqualand West, South Africa, is composed of early Paleoproterozoic-age mixed siliciclastic and iron formation strata from a marine deltaic

system on the western margin of the Kaapvaal craton (Beukes 1978, Schroeder et al. 2011; Fig. 1). Strata of the Koegas Subgroup are composed of interbedded deltaic tongues of siliciclastic deposits and granular and banded iron formation, with current and wave-ripple cross-stratification and lower plane bed laminations, respectively. The siliciclastic sediments were fed by a river system that reflects the uplift and erosion of much of the pre-Koegas strata across the Kaapvaal Craton, and ended a 100-million year interval of deposition of largely chemical sediments (carbonates and iron formation) across the craton (Schröder et al., 2011). The abundance of potassium feldspar, monazite and zircons (e.g., Fig. 4) suggest a felsic igneous source for the Koegas sediments, and paleocurrent and sequence stratigraphic data indicate a sediment source to the east, as the deltaic strata prograde to the west and northwest (Schröder et al., 2011). Taken together, these observations suggest either the removal of a substantial thickness (>2 km) of flat-lying sedimentary cover (iron formation and carbonate; see Fig. 2 and previous text) from the central platform to expose Ventersdorp or older bedrock or, perhaps more likely, materials were sourced from a magmatic arc to the east of the Kaapvaal Craton (Schröder et al., 2011). Geological constraints on the sediment provenance thus suggest transport from at least the central Kaapvaal craton (>300 km) or across the entire craton (>1000 km), with either possibility recording a substantial craton-scale river system delivering materials to the Koegas sedimentary basin. Iron formation facies developed during intervals and in areas with low relative siliclastic input. The iron formations are diverse mineralogically, with laminations composed of intimate and gradational mixtures now composed of microcrystalline hematite, siderite, magnetite, and iron silicates. Zircons

from an ash bed in the Rooinekke Formation of the Koegas Subgroup were dated to 2415 ± 6 Ma (Gutzmer, Jens and Beukes, Nicolas, 1998). Other known ages are consistent with this date (Fig. 2), with the underlying Kuruman and Griquatown formations dated at 2460 ± 5 Ma and 2432 ± 31 Ma, respectively (Pickard, 2003; Trendall et al., 1990; Nelson et al., 1999), and with the overlying Ongeluk Formation constrained to 2222 ± 12 Ma (Cornell et al., 1996).

Drill cores capturing Koegas Subgroup strata were retrieved by the South African Agouron Drilling Project in 2006 (Fig. 3; (Schröder et al., 2011; Johnson et al., 2013). Drill core materials are important here because the surface of southern Africa has not been glaciated since Permian time and is deeply weathered by oxidative chemical weathering processes that have impacted sandstones as well as iron formations. One core (GTF-01) was drilled in a proximal location in the Koegas basin, while a second core (GEC-01) was collected downdip in more distal facies that lack siliciclastic units of sufficient grain size that can be examined for redox-sensitive detrital grains, such as sandstones and conglomerates. A previous report described the stratigraphy and sedimentology of the Koegas Subgroup, including the lithostratigraphy of GTF-01 (Schröder et al., 2011). We present a similar stratigraphic column, slightly revised to reflect our petrographic work that re-described several intervals originally marked as sandstones as cross-stratified granular iron formation (Fig. 3). The general stratigraphy captured by the drill core records a dynamic interplay between iron formation and terrigenous siliciclastic deposition (Fig. 3). The contact between the lowermost unit

Koegas Subgroup, the Pannetjie Formation, and the underlying Griquatown Iron Formation is sharp and associated with a thin, 10 cm-thick conglomerate of iron formation clasts (Beukes and Gutzmer, 2008). The Pannetjie Formation marks the onset of widespread delivery of siliciclastic sediments to the basin, and is composed of shale to very fine-grained sandstones. The thin, overlying Doradale Formation begins with a coarse bed of granular iron formation, and then is mainly finely laminated mixtures of ferrous and ferric-rich iron formation with abundant diagenetic chert and carbonate nodules. The Naragas Formation, starting around 250m depth, begins with another influx of siliclastic deposits corresponding to the progradation and lobe switching of an ancient delta. We observed a thin (<10 m) unit of deeper iron formation in the thick ~100 m Naragas Formation, but as Schröder et al. (2011) noted, this formation is mainly comprised of cross-stratified detrital deltaic sandstones. The abundance of fine to medium-coarse sandstones, with common quartz and feldspar grains and occasional detrital zircon and monazite and interbedded with shales, presented ideal targets for redox-sensitive grain investigation. The overlying Heynskop Formation begins as mainly mixed ferric and ferrous iron formation with chert nodules and thin sandstone beds. The Heynskop then shallows in the upper half, first with beds of granular iron formation, then shale, and finally ~5 m of sandstone beds. Above the sandstones, there is a rapid deepening, including a brief ~1 m-thick microbially-textured carbonate-rich bed before banded iron formation deposition resumes in the Rooinekke Formation. From point count data of thin sections, Schröder et al. (2011) characterized the Heynskop and Naragas sandstones as subarkosic.

In a previous study, we noted the presence of detrital pyrite and confirmed its detrital and distinct origin from authigenic pyrite using *in situ* measurements of multiple sulfur isotopes (Johnson et al., 2013). Here we explore in depth the sandstone intervals from the Koegas Subgroup using the GTF-01 core and report the discovery of detrital uraninite and a characterization of the detrital pyrite abundance in representative petrographic thin sections of sandstone beds throughout the drill core.

Methods

Sandstone units from throughout the Koegas Subgroup were investigated for oxygen-sensitive pyrite and uraninite grains using light and electron microscopy of microprobe-quality polished thin sections. We focused on the thickest sandstone interval, which was deposited in the upper Naragas Formation, with several smaller intervals in the lower Naragas and in the Heynskop formations (Fig. 3). Twenty billets approximately 27 x 46 x 5 mm in size were cut from the core using a rock saw, sampling sandstones at 76-84 m (10 billets), 158-190 m (6), 203 m (2), and 243 m (2). These were then made into 30 μ m-thick thin sections and polished to obtain a microprobe quality surface. Thin sections were subsequently examined and mapped on a Leica polarizing microscope using reflected and transmitted light microscopy. Samples containing abundant well-rounded pyrite grains identified using reflected light microscopy were then carbon coated with 7-15 nm using a Cressington Carbon Coater in preparation for study on the scanning electron microscope (SEM) and electron microprobe (E-probe).

Pyrite and uraninite were identified and imaged on a Zeiss 1550 VP Field Emission Scanning Electron Microscope (SEM) using an attached Oxford INCA Energy 300 X-ray Energy Dispersive Spectrometer (EDS) system. Coated samples were set at a working distance of 8 mm and probed with a 15 keV electron current. $K\alpha$ X-ray fluorescence measurements used energy-dispersive spectroscopy to confirm phase identification, with quantitative elemental analyses providing relative accuracy of 5% or better. Grains were photographed on the SEM using the backscatter electron detector mode to enhance compositional contrast. For cathodoluminescence (CL) imaging, the detector was set on Variable Pressure Secondary Electron at a working distance of 10mm, and photographs were taken to assess grain shape and abrasion by truncation of internal zonation in feldspar and quartz grains.

To measure the abundance of detrital pyrite, elemental maps of four representative sections were produced using a JEOL JXA-8200 Advanced Electron Probe Micro-analyzer (E-probe) equipped with tungsten and LaB6 electron sources and five wavelength dispersive X-ray spectrometers (WDS). Intensity maps of sulfur, zirconium, and phosphorus abundance were measured over approximately 90% of the thin section area to determine heavy mineral compositions of the sandstones (relative abundance of pyrite, zircon, and apatite+monazite, respectively). The data matrices were reduced using a scaling function to select significant concentrations of S, P, and Zr. The abundance of pyrite, zircon, and apatite+monazite were determined by calculating the fraction of area

they occupied and adjusting for porosity (estimated visually to be 20%, within a normal range for sandstones; Boggs, 2006) (Table 2). These estimates are subject to similar logical uncertainties as classic point counting, but our use of E-probe produced elemental maps should eliminate human counting and identification errors and biases.

Results

Redox-sensitive detrital grains were definitively identified in every sandstone bed we examined from the Koegas Subgroup (Fig. 3). The most common grains, quartz and feldspar, varied from sub-angular to well-rounded (Folk, 1957) and were fine to medium sand in size (after Wentworth, 1922). Both quartz and feldspar show compositional zonation highlighted by cathodoluminescence, with abundant evidence of truncation by physical abrasion (Fig. 4). Detrital pyrite grains were also common (Fig. 4, 5, 6). These can be distinguished from authigenic pyrite using a series of qualification standards (Rasmussen and Buick, 1999). Detrital grains occur as clear sedimentary grains in grain-supported sandstones. The grains themselves have rounded profiles, distinct grain boundaries, and inclusions of other mineral phases, and are commonly hydrodynamically concentrated with other heavy (i.e., dense) mineral grains such as zircon and apatite (Fig. 5, 6). Quantification of the relative abundances showed that the amount of pyrite generally scales with zircon and apatite+monazite, with the exception of an especially pyrite-rich sandstone sample at 77 m (Table 2). Some detrital pyrite grains show grain-boundary truncations (Fig. 6) and frequently the pyrite is concentrated on heavy mineral bands associated with cross-bed foresets (Fig. 5). Because of density differences (quartz

= 2.66 g/cm³, potassium feldspar/orthoclase = 2.56 g/cm³, pyrite = 5 g/cm³) pyrite grains in hydraulic equilibrium are smaller (very coarse silt to very fine sand, when converted from 2D spherical segments to 3D spherical diameters; Kong et al., 2005) and more rounded (rounded to well-rounded; Folk, 1957) than surrounding quartz and feldspar sand grains. These detrital pyrite grains are easily differentiated from authigenic pyrite derived from post-depositional fluids, which precipitate as euhedral to subhedral crystals or in overgrowth, pore-filling, and replacement textures. The detrital grains show no signs of weathering rinds or reaction rims, which might occur if chemical erosion occurred (from dissolved oxygen) in addition to physical abrasion. This implies that physical abrasion was the dominant (and perhaps only) component of grain erosion.

Detrital uraninite is far more rare and was only detected from a thin section at 203.65m in GTF-01 (Fig. 6j). The uraninite has since undergone radioactive decay and been altered to uraninite-uranothorite (UO₂-U,ThSiO₄) with galena and bitumen inclusions. This mineralogy and auto-brecciation is expected from an original uraninite grain as radioactive decay of uranium yields helium, thorium, and lead as daughter products. The addition of helium causes structural strain, and its release along grain boundaries causes crack development and produces a paths for interaction with later fluids (Ono, 2001). Later, sulfur-bearing fluids reacted with radiogenic lead to produce the galena inclusions observed (Ono, 2001). Because galena has a larger molar volume than uraninite (31.5 cm³/mol vs. ~24.6 cm³/mol), this also promotes fragmentation of uraninite (Finch and Murakami, 1999; Ono, 2001). Coffinization of uraninite, or diagenetic replacement of

uraninite with coffinite (USiO_4), is a common reaction when reducing fluids with high silica activity are present (Janeczek and Ewing, 1992). Additionally, mobile hydrocarbons are known to solidify from radiation-induced polymerization as bitumen solids (i.e., radiobitumen) in and around the uraninite, which subsequently enhances the dissolution and fragmentation of the uraninite grain (Janeczek and Ewing, 1992; England et al., 2001). The presence of each of these features in the Koegas Subgroup allows the confident identification of detrital uraninite in addition to detrital pyrite.

We did not observe any clear examples of detrital carbonate grains, including siderite. Two examples from the literature of detrital siderite grains (Table 1, (Rasmussen and Buick, 1999)) likely underwent less weathering. With the longer transport distance of the Koegas sediments, any softer siderite grains (Moh's hardness = 3.5 to 4.5)—which are also substantially more susceptible to chemical dissolution from meteoric waters—eroded while the sturdier pyrite and uraninite grains survived (Moh's hardness = 6.5 and 5 - 6, respectively).

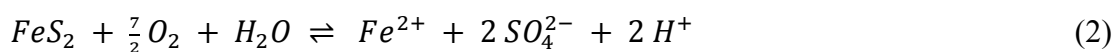
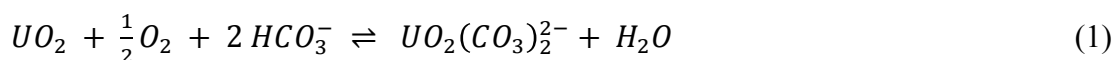
The discovery of uraninite and pyrite detrital grains in the Koegas Subgroup is interesting in light of the overall geologic context of the Transvaal Supergroup and constraints on the timing of the rise of oxygen. With the pyrite- and uraninite-bearing Black Reef Quartzite Formation at the base of the Transvaal Supergroup, the discovery of redox-sensitive detrital grains throughout the overlying Koegas subgroup neatly brackets the long-lived Campbellrand-Malmani carbonate platform between two siliciclastic successions

deposited under low O₂ conditions (Fig. 2). Our observations of (abundant) detrital pyrite and (more rare) detrital uraninite further suggest that at 2.415 Ga, the O₂ levels were not sufficiently high to oxidize these minerals during weathering and transport and remove them from the record. The presence of detrital pyrite and uraninite at 2.415 Ga marks the youngest redox-sensitive detrital grains currently known with geochronological constraints, setting an upper age for the Great Oxidation Event.

COMBINING PHYSICAL AND CHEMICAL WEATHERING PROCESSES TO CONSTRAIN ANCIENT O₂ LEVELS

Redox-sensitive detrital grains present a simple and attractive proxy for O₂ in Earth surface environments. They are easily observed and the mechanics behind their preservation in fluvial and nearshore marine conglomerates and sandstones are known. A remaining challenge concerns how observations of detrital pyrite and uraninite in a given sedimentary context translate into quantitative constraints of the amount of O₂ present in the environment. The presence of these grains during weathering and physical transport indicates low O₂ levels, but how low is low? Very few sedimentary redox proxies (many of which are marine in concept) exist that can be directly inverted for O₂ concentrations. To provide new insight into this problem we developed a mathematical framework that captures the processes that destroy detrital pyrite and uraninite grains by coupling chemical weathering rates to physical processes that abrade grains with insight from process sedimentology (e.g., Sternberg, 1875; Sklar et al., 2006; Le Bouteiller et al., 2011).

The rates of chemical weathering of pyrite and uraninite and their sensitivity to oxygen levels have been studied (Grandstaff, 1976, 1980; Williamson and Rimstidt, 1994; Ono, 2001), with O₂ estimates derived solely from the chemical dissolution rate laws of these redox-sensitive minerals. In principal, both the chemical weathering of uraninite and pyrite are sensitive to oxygen (Holland, 1984; Stumm and Morgan, 1996), as shown at pH ≥ 6 as:



Laboratory rate laws have been constructed for both O₂-dependent dissolution reactions. Grandstaff (1976) produced a chemical oxidation rate law for uraninite based on experiments oxidizing insoluble uraninite to soluble uranyl ions, with dissolution dependent on surface area, pH, organic compounds, the amount of non-uranium cations, the total dissolved carbonate, the temperature, and the dissolved oxygen content. From the rate law, estimates were applied to riverine conditions of organic content, cation content, CO₂, temperature, alkalinity, residence time, and grain specific surface area for the Witwatersrand and Elliot Lake deposits (Grandstaff, 1980). Surface areas were chosen using the average grain diameters found in these deposits (75 μm) and Precambrian atmospheric estimates of 5 to 100 times the present levels of carbon dioxide or 0.0016 to 0.032 atm CO₂. An average temperature of 15°C and travel distance of 10 to

500 km from earlier estimates of these deposits were used (McDowell, 1957; Hallbauer and Utter, 1977). Noting that the average sediment transport velocities of the Mississippi and Columbia rivers were on the order of 1 km yr^{-1} , Grandstaff (1980) decided the Witwatersrand and Elliot Lake deposits had higher velocities of $1.5\text{-}7.5 \text{ km yr}^{-1}$ based on their larger average grain size. Yet since sediments often reside temporarily in alluvial deposits, drastically increasing their residence time by tens of thousands of years, they could also be potentially exposed to oxygen for thousands of years or more before removal from the source rock and after deposition. These varying time intervals of sediment storage were accounted for by inputting variable amounts of residence times for soil, river, and depositional time periods, from 600 to 110,000 years. Together, these estimates allowed Grandstaff to use his chemical dissolution rate law to invert for paleo-oxygen levels (Grandstaff, 1980).

Grandstaff deduced that for uraninite to be present in Archean and Paleoproterozoic siliciclastic deposits, ancient O_2 concentrations must have been less than $\sim 2.1 \times 10^{-3}$ to 2.1×10^{-6} atm (Grandstaff, 1980). At the lowest CO_2 levels he considered, ancient O_2 constraints were higher, from around 0.001 atm to 0.0001 atm, while higher carbon dioxide levels (100 times our preindustrial atmosphere) decreased the O_2 constraints to closer to 1×10^{-5} and 1×10^{-6} atm. Though the CO_2 levels of the early atmosphere remain somewhat poorly constrained and a topic of substantial debate (e.g., Rye et al., 1995; Sheldon, 2006), more recent estimates suggest an early atmosphere with even higher CO_2 levels of approximately 0.03 to 5 atm, with an upper bound of 0.3 atm by early

Proterozoic time (Grotzinger and Kasting, 1993; Halevy et al., 2009). Furthermore, these previous calculations assumed physical erosion processes consumed half the mass of a detrital uraninite grain without incorporating rules for physical abrasion. Grandstaff was also careful to point out that these estimates are upper bounds as they do not take the potential impacts of uraninite-oxidizing microbes into account, as biologically driven catalysis of this reaction would occur at faster rates for a given O_2 concentration (Grandstaff, 1980).

A rate law was similarly produced for the chemical weathering, or oxidation at neutral pH, of pyrite by O_2 using a compilation of measured (defect-free) pyrite oxidation rates (Williamson and Rimstidt, 1994), with the dissolution solely dependent on pH and dissolved oxygen. Estimates of O_2 following this pyrite oxidation rate law have suggested a constraint of approximately 2.1×10^{-6} atm when detrital pyrite is found (Anbar et al., 2007; Reinhard et al., 2009). As these rates are for pyrite free of defects, using this law provides an upper boundary for O_2 estimates, as natural pyrite samples would likely oxidize at higher rates (Anbar et al., 2007; Reinhard et al., 2009). One study applied this rate law to a very fine sand-sized (side length = 100 μm) cubic pyrite crystal under a range of pH and oxygen levels and found that oxidation was extremely slow at $O_2 \sim 1 \times 10^{-14}$ atm, taking 100 million years or more to dissolve the crystal (Reinhard et al., 2009). However, at O_2 levels near the upper constraints from multiple sulfur isotopes, $\sim 2.1 \times 10^{-6}$ atm (e.g., Pavlov and Kasting, 2002), dissolution was much more rapid, taking only tens of thousands of years (Reinhard et al., 2009). In a similar application, Anbar et al. (2007)

used Williamson's rate law to determine that a similarly-sized pyrite crystal would dissolve at $\sim 2.1 \times 10^{-6}$ atm in less than 20,000 years (Anbar et al., 2007). Both of these calculations aimed to demonstrate how oxidative pyrite weathering might occur at ca. 2.5 Ga even at exceedingly low oxygen concentrations, and they highlight the sensitivity of pyrite to very low O_2 levels, albeit at small initial grain diameters.

No previous work has combined these chemical weathering rate laws with models of physical erosion to assess the conditions required for preservation of redox-sensitive detrital grains in the geological record. It is certain that physical abrasion of sediment particles occurred during sediment transport, as evidenced by the rounding of particles and their occurrence in sedimentary structures that indicate transport (at least regionally) in bedload (Fig. 5, Fig. 6). It is crucial, therefore, to incorporate physical erosion into models of grain survival to arrive at higher quality constraints on paleoenvironmental O_2 concentrations.

The presence of redox-sensitive detrital grains will be sensitive to the amount of physical abrasion, which relates in the simplest sense to the distance the grain has traveled, as well as the amount of chemical weathering, which reflects the total time of exposure and the amount of oxygen. We treat sedimentary grains as spheres and rewrite the previously derived chemical oxidation rate law for uraninite (Ono, 2001; Grandstaff, 1980) to produce an expression in terms of radial erosion rate (R_{uran}) in meters per year:

$$R_{uran} = 6.29 \times 10^{21} (RF^{-1}) (10^{-10.8NOC}) (\Sigma CO_2) (H^+) (pO_2) \exp\left(\frac{-7045}{T}\right) MW_u \rho^{-1}, \quad (3)$$

where RF is the organic retardation factor, NOC is the mole fraction of non-uranium cations in uraninite, ΣCO_2 is the total dissolved carbonate, pO_2 is atmospheric oxygen in PAL, T is the absolute temperature, MW_u is the molecular weight of uraninite, and ρ is the uraninite density, 11 g cm^{-3} . We set $RF = 20$ for a mid-range organic retardation factor, $NOC = 0.17$ for a mid-range cation mole fraction, and $T = 298 \text{ K}$ or 25°C (Grandstaff, 1980). We used 0.1 atm as a mid-range value of ancient CO_2 estimates for the early Proterozoic atmosphere (Grotzinger and Kasting, 1993).

Similarly, for pyrite dissolution, the equation of Williamson and Rimstidt (1994) can be rewritten in terms of radial erosion rate (R_{pyr}) in meters per year:

$$R_{pyr} = 0.135 (DO^{0.5}) MW_p \rho^{-1} (H^+)^{-0.11}, \quad (4)$$

where $\rho = 5.01 \times 10^6 \text{ g m}^{-3}$, $MW_p = 119.98 \text{ g mol}^{-1}$, and DO is the dissolved oxygen content in mol L^{-1} .

To incorporate physical weathering, we applied Sternberg's Law, which describes the widely observed exponential reduction of particle diameter with transport distance due to abrasion of particles (Sternberg, 1875):

$$D = D_0 \exp(-x/x_0) , \quad (5)$$

where D is particle diameter at distance x , D_0 is the initial diameter, x is the distance grain has traveled, and x_0 is a material specific length scale of erodability (Sternberg, 1875). The term x/x_0 describes the transport distance relative to the characteristic distance to radially erode a grain by a factor of e . This model for physical abrasion of grains is widely used (Lewin and Brewer, 2002; Sklar et al., 2006; Le Bouteiller et al., 2011).

Combining both physical abrasion and chemical weathering yields an equation for grain-size evolution, with physical erosion as a function of transport distance and chemical weathering as a function of time (t):

$$D = D_0 \exp(-x/x_0) - R t , \quad (6)$$

where R denotes the chemical weathering rate for either grain designated. We note that this model implicitly assumes that physical and chemical erosion rates are independent and additive, which may not be true. Several recent studies have shown that physical abrasion exposing new surfaces is an important control on chemical weathering rates, revealing these two processes are tightly coupled (Riebe et al., 2003; Ferrier and Kirchner, 2008). Thus O_2 estimates from our approach should be treated as conservative constraints, because in more realistic scenarios physical and chemical erosion would feedback on and amplify each other. Nevertheless, this model determines an upper bound on ancient O_2 concentrations and a lends stepping-stone for future modeling efforts once

the feedbacks between chemical and physical weathering are quantitatively realized for different redox-sensitive detrital minerals.

We seek to obtain this upper bound on oxygen levels using redox-sensitive grain survival; therefore, we are interested in the time it takes for a given grain of pyrite or uraninite to become effectively undetectable in the sedimentary record as a function of O_2 concentrations. We assign a critical grain diameter (D_{cr}) set at 10 μm —a size below which grains are too small to uniquely and routinely distinguish detrital from authigenic phases in a siltstone or shale. Setting D equal to D_{cr} in equation (6), dividing the equation by D_{cr} and rearranging results in:

$$R t / D_{cr} = \left(D_0 / D_{cr} \right) \exp(-x/x_0) - 1 \quad (7)$$

Equation (7) contains three important dimensionless parameters. The term on the left hand side of the equation represents the total amount of chemical weathering relative to the critical grain diameter, which we rename for convenience as:

$$r_c = R t / D_{cr} \quad (8)$$

The second dimensionless parameter is the initial sediment diameter as compared to the critical ‘undetectable’ size (D_o/D_{cr}), and the third parameter is the total transport distance relative to a material-specific erodibility length constant (x/x_o).

The erodibility length coefficient, x_o , is not well-known for pyrite and uraninite. Measurements of x_o have produced variable results depending on experimental design. One study found that for 0-128 mm sieved river sediments, the erodibility coefficient varied from 50 to 333 km using abrasion experiments (Mikoš, 1995). Another experimental investigation using slightly weathered chert grains measured a larger range of erodibility coefficients, from 8 km to 794 km (Kodama, 1994). However, a study of rivers in Canada determined that many laboratory abrasion experiments underestimate the erodibility coefficient, finding that quartzite, limestone, and granitic sediments varied from 333 km to 925 km (Shaw and Kellerhals, 1982). These workers suggested that because coarse grains are often “at rest”, the estimates of abrasion from laboratory abrasion mills predict too small x_o (Shaw and Kellerhals, 1982). Earlier laboratory studies using less vigorous abrasion techniques determined erodibility coefficients for chert of ~1000 km to 10,000 km (see Kodama, 1994 for a compilation). Indeed, sediments at the deltas of long continental-scale rivers such as the 6650 km Nile River would indicate that the erodibility coefficient of these sediments is greater than a few hundred kilometers, or that fluxes of new large grains enter the river to replenish the comminuted sediment (e.g., Sklar et al., 2006). In addition to material properties, x_o might also depend on the mode of transport (e.g., bedload versus suspended load) and particle size. For example, particle-

bed impacts are viscously damped for small particles with low impact velocities. Using a Stokes number threshold of 30 for viscously damped impacts (Schmeeckle et al., 2001; Joseph and Hunt, 2004), we find that particle-bed impacts from dense pyrite and uraninite grains can be damped for diameters finer than fine- to very-fine sand when falling in still water, thereby effectively increasing x_0 . However, particle velocities can increase substantially in turbulent flow due to suspension (e.g., (Lamb et al., 2008)), so that even silt-sized grains still erode depending on the transport mode. No estimates of the erodibility coefficient of pyrite or uraninite have been measured, but the relatively similar Moh's hardness for quartz (7), uraninite (5-6), and pyrite (6.5) suggests similar erodibility coefficients. To keep our analysis tractable for analyzing ancient rocks, we employ a constant x_0 of 1000 km for both pyrite and uraninite for comparison when dimensionalizing equation (7). Note that while we will discuss the dimensionless parameter x/x_0 as increasing by distance traveled, the term can also be thought of as increasing with more erodible material or more energetic grain-to-bed impacts (i.e., smaller x_0).

To determine a set of practical r_c values, we used physical constraints on the initial grain sizes and final distances traveled. We chose a range of reasonable initial grain sizes, varying from $D_0 = 5$ mm (e.g., from an igneous source) to $D_0 = 20$ μm similar to a disseminated sedimentary pyrite source. We later input conservative r_c values for D_0 up to 5 mm for pyrite grains as these are often found in Archean conglomerates at 1-2 mm (England, 2002) but used a maximum of 1 mm for uraninite grains, which are commonly

observed to be smaller in conglomerates, maximally ca. 100 μm (England et al., 2001). Dividing by D_{cr} (10 μm), the parameter D_0/D_{cr} therefore varies from 1 to 500. Total travel distances were set to range from 10 to 10,000 km, encompassing short-transport systems such as Malibu Creek, CA (22 km) to long continental rivers such as the Mississippi River (3734 km) and the Nile River (6650 km). When divided by an x_0 of 1000 km, the x/x_0 parameter has a range of 0.01 to 10. Under these transport conditions, spanning reasonable ranges in initial sizes and total travel distances, r_c values were calculated to show the ranges and relationships between these variables in equation (7) (Fig. 7A). Note that choosing a different erodibility coefficient (x_0) simply shifts the solution space either right or left, but the range of r_c needed to fill the parameter space remains similar.

Figure 7A shows that for x/x_0 less than ~ 0.1 (i.e., transport distances less than 100 km with $x_0 = 1000$ km), only the initial grain size D_0 is relevant for determining the erosion rate. Chemical erosion dominates this domain: r_c is essentially constant for a given D_0 and there is no relationship between amount of chemical erosion and relative travel distance or x/x_0 . This solution space encompasses previous work on the chemical erosion rates of redox-sensitive detrital grains where physical erosion was neglected. Such high rates of chemical erosion consequently require higher levels of O_2 .

As x/x_0 increases from mid-length streams (like the Hudson River, 507 km) to transcontinental rivers (like the Mississippi River, 3734 km), physical erosion becomes more important (Fig. 7A). At these large transport distances, the initial grain size

becomes less determinate and distance traveled is a larger factor in grain survival. Lines of low r_c at large total travel distances (large x/x_0) represent extensive river systems with grains abrading under low chemical erosion. This is likely the case for grains preserved in the proximal part of the basin during deposition of the Koegas Subgroup, which likely traversed much of the Kaapvaal craton (Sumner and Beukes, 2006; Schröder et al., 2011). For these larger river systems, Figure 7A illustrates that chemical erosion and physical abrasion are both important factors in grain survival.

To help conceptualize the factors that affect the relative chemical erosion (r_c), we produced two plots showing r_c when one parameter (either the relative initial grain size or the relative distance) is held constant. The solution shown in Figure 7B, and in Figure 7A as a dashed line marked “(B)”, demonstrates how the portion of chemical erosion changes with increasing distance for a set grain size (in this case, a diameter of 1 mm). At short distances, a large amount of chemical erosion is required to erode the 1 mm grain to the critical diameter of 10 μm —implying that a high level of oxygen is also required to generate this high degree of chemical erosion. At longer distances, however, physical abrasion increases and relative chemical erosion decreases, resulting in lower and lower r_c values. At around 4500 km, physical abrasion erodes nearly all of the grain, and thus no chemical erosion is needed to explain the absence of grains larger than 10 μm . At larger distances (shaded in grey), physical abrasion is so strong that 1 mm grains would not have survived to these distances at a size above our detectable limit of 10 μm .

Figure 7C, shown in Figure 7A as a dashed line marked “(C)”, illustrates the grain size control under a set travel distance of 1000 km. Grains beginning at diameters of $\sim 30 \mu\text{m}$ or smaller would no longer exist after 1000 km of travel. Particles starting at $\sim 100 \mu\text{m}$ or smaller would require very little chemical erosion as physical abrasion would cause most of the grain destruction, although viscous damping may reduce physical abrasion rates for these small sediment sizes depending on the transport mode. As the initial grain size increases, the relative amount of chemical erosion necessary for grain destruction also increases, and large grains several millimeters in diameter would require a large degree of chemical erosion to be destroyed by 1000 km of travel.

Because the relative amount of chemical erosion, r_c , is environmentally controlled, estimates of the ancient r_c for specific deposits can be informed by the sedimentary context of the redox-sensitive grains. Observable differences in grain sizes, chemistry, provenance, sedimentary structures, basin size, and sequence stratigraphy can be applied to inform transport conditions (distances and times) and thus O_2 constraints. Armed with estimates of the transport conditions, one can estimate an appropriate range of r_c values for a given sedimentary deposit bearing detrital pyrite or uraninite grains.

As r_c is a function of the oxygen-dependent chemical erosion for both pyrite and uraninite, the dissolved oxygen (*DO*) content of weathering fluids (river water, ground water, pore fluids in soils and sediments, and seawater) can be constrained using both the uraninite and pyrite erosion equations, yielding predictions of O_2 (in atm) from both

minerals, assuming gas exchange equilibrium. We input r_c values previously determined using reasonable but conservative ranges of D_0/D_{cr} and x/x_0 (Fig. 7A). We used a range of 0 to 300 for pyrite, as it commonly has larger initial grain sizes, and 0 to 150 for uraninite. We solved Eqn. 8 for O_2 , using the appropriate rate laws for pyrite and uraninite (Eqn. 3, Eqn. 4), inputting a typical riverine pH of 6, modern CO_2 values (Fig. 8A) and a mid-range paleo- CO_2 estimate of 0.1 atm (see previous discussion, Fig. 8B). These functions denote oxygen concentrations required for grain erosion to 10 μm (D_{cr}) for a given amount of time (Fig. 8). A model calculation for current day conditions has modern oxygen levels marked, indicating where pyrite and uraninite grains would be stable under today's atmosphere (Fig. 8A). According to these estimates both pyrite and uraninite appear to be stable (as long as the initial grains are large enough) for about 10,000 years under today's atmosphere. Modeling ancient atmospheric conditions shifted the uraninite destruction field considerably but did not alter the O_2 requirements for pyrite grain destruction, because of the CO_2 dependence of uraninite dissolution (Fig. 8B; Eqn. 3). Changing the pH of weathering fluids to 5 causes estimates based on pyrite to vary imperceptibly while this change decreases the uraninite upper bounds by approximately an order of magnitude. At pH = 7, pyrite constraints on O_2 similarly do not significantly change but uraninite O_2 constraints are relaxed by a factor of ten, increasing the maximum oxygen levels that are allowed by the preservation of detrital uraninite grains.

Because the O_2 estimates indicate the oxygen levels where pyrite and uraninite should be undetectable, these calculated levels can be used as the maximum oxygen levels at which pyrite and/or uraninite will still survive and be recognizable detrital components of a clastic sedimentary rock. The O_2 constraint estimates are shown for a range of solutions that account for the diversity of environments and transport regimes affecting sediment supply and physical erosion (i.e., ranges of expected D_0 and x). The time allowed for grain destruction is also a corollary of different paleoenvironments and deposit types, as these relate to travel time. The ranges marked with r_c values show the influence of physical conditions, such as initial grain size and total distance traveled, with higher r_c corresponding to a higher degree of chemical erosion and lower r_c representing lower proportion of chemical erosion. Higher r_c would be anticipated for rivers with low total travel distance and larger initial grain sizes like proglacial or coastal mountain streams (left side of Fig. 8B marked “Short Rivers”). Lower r_c represents a lower proportion of chemical erosion and more physical erosion, with smaller saltating grains and larger total travel distances like in large continental river and delta systems (right side of Fig. 8B marked “Long Rivers”). Figure 7A suggests that the highest levels of chemical erosion would not allow pyrite and uraninite grains to still be present at long distances. Thus, longer continental rivers such as the Mississippi can only have r_c values up to ~ 5 (Fig. 7A). Consequently, in our longer river estimates, we conservatively constrain r_c to be 50 or less.

We can also add time constraints on different river system types using recent work applying U-series disequilibrium techniques to measuring sediment transport times. Transport time starts when the grains are first excised from their source bedrock, and integrates both the time the sediments spend being transported and their temporary storage on hillslopes and in floodplains, on the riverbed and in fluvial bedforms (like bars). As U and Th have different mobility and are consequently fractionated during initial weathering from bedrock in secular equilibrium (i.e., a closed system for > 1 million years), the degree to which this isotope decay series is in disequilibrium can be inverted to calculate the time since initial removal from source bedrock (Chabaux et al., 2003; DePaolo et al., 2006; Dosseto et al., 2008). This technique has been applied to both the suspended load and bedload of several rivers. In mountain streams, cobbles and boulders are typically in bedload, and consequently they have longer transport times than the suspended and dissolved load. The <5 mm pyrite and <1 mm uraninite mineral grains would be in the suspended load in such systems. Measurements in short rivers have ranged from mountain streams in the Andes to Icelandic glacial streams, where the suspended sediment load transport time has been measured at 3 to 4 kyr in the ~200km Andes tributaries (Dosseto et al., 2006) and 1 to 10 kyr in short Icelandic rivers (~40-200 km) (Vigier et al., 2006). In a different type of measurement, Lauer and Parker (2008) modeled a tracer from mining contamination to estimate the transport of clay and silt (the suspended load) of the upper ~70 km of the Clark Fork River would take thousands of years (Lauer and Parker, 2008). We therefore posit that mountain, glacial, and shorter rivers (1000km or less) will have total transport times of 1000 to 10,000 years, and add a

label to Figure 8 for 'Short Rivers' to constrain the oxygen levels from finding detrital uraninite and pyrite from these river systems.

Larger rivers with broad floodplains have much longer grain transport times (e.g., Bradley and Tucker, 2013), and this distance-time relationship is enhanced by the transport mode. In rivers such as the Mississippi or Nile, sandy bedforms indicate that sand-sized particles travel in bedload and silt-sized grains are typically in suspension. Figure 7A indicates that at these long distances all preserved grains likely started >500 μm in diameter. These grains probably started out in hillslopes, first weathering from bedrock, and then were transported in mountain streams as suspended load, and finally as bedload in larger rivers. Only a few studies have examined the bedload transport time using the U-series method. For example, Granet et al. (2010) determined that the transport time from the Himalayas to the Ganges delta in Bengal (Manihari, India) was >300 kyr for bedload grains to move ~2200 km. They also studied the bedload of Himalayan feeder streams (650-1000 km) and estimated that transport time from the source bedrock to the confluence with the main Ganges river was ~100 kyr (Granet et al., 2007). These are significantly longer than estimates for the suspended sediment load, where only 20-25 kyr was measured for these shorter Himalayan feeder streams (Granet et al., 2010). Another study found a similarly short transport time (10 to 28 kyr) for the suspended sediments of the ~1700 km Mackenzie River in Canada (Vigier et al., 2001); however, the authors noted that erosion in this river system was affected by recent glaciations. Dosseto et al. (2006) observed that in Amazon lowland rivers, the suspended

load took 100 to 500 kyr to travel 760 km to several thousand km. We therefore suggest that for long, > 1000 km river systems, total sediment transport time ranges from 100 to 500 kyr. While the U-series approach is still being refined (e.g., see Lee et al., 2010; Handley et al., 2013), we applied these estimates of bedload transport time (i.e., 1 kyr to 10 kyr for short river systems and 100 kyr to 500 kyr for long river systems) to compare depositional environments (Fig. 8).

With these timing constraints of river sediment transport and our estimates of r_c , we can place upper boundaries on ancient oxygen levels. Short rivers, such as mountain or glacial streams, show some pyrite being stable up to O_2 concentrations of 40 atm, or ~ 190 times the oxygen content of the modern atmosphere. Finding detrital uraninite in ancient mountain (cobble-bedded) rivers, however, constrains the atmospheric oxygen levels to a maximum of 10^{-2} atm. Longer river systems with small initial grains and long transport distances, like the Amazon or Mississippi rivers, constrain O_2 to much lower levels. The presence of both pyrite and uraninite in these systems implies an upper limit of ancient O_2 on the order of $1 \cdot 10^{-5}$ or $1 \cdot 10^{-6}$ atm, with all pyrite being destroyed before $1 \cdot 10^{-4}$ atm and uraninite no longer preserved at $3.2 \cdot 10^{-5}$ atm. Thus, if grain provenance and/or travel distance for an ancient river system can be determined, the presence of redox-sensitive detrital grains can provide powerful redox constraints.

For our study area, the deltaic sediments of the Koegas Subgroup, our model provides a mechanism to determine an upper bound on the paleo-oxygen levels. For a craton-scale

sediment transport system (ca. 1000 km, our best estimate for Koegas provenance), we can use the estimates at ~100,000 years to predict a maximal oxygen level of 3.2×10^{-5} atm at 2.415 billion years ago. This estimate is an upper limit for the largest pyrite and uraninite grains to be preserved: for all pyrite and uraninite particles to be preserved, oxygen levels can be constrained to more like 1×10^{-7} atm. As we do not observe reaction rims suggestive of chemical erosion, this lower estimate may be a more appropriate upper bound for Earth surface O₂ levels at this time.

DISCUSSION AND CONCLUSIONS

Detrital uraninite and pyrite have long been recognized and interpreted as a robust but qualitative measure of low O₂ levels on the early Earth. In the context of our combined chemical and physical erosion framework, the preservation of these grains in Archean and early Paleoproterozoic siliciclastic sedimentary rocks (like those in the Koegas Subgroup) can be viewed through a more quantitative lens. We examined the plausible range of O₂ values necessary to erode (to a critical diameter set at 10 μm) pyrite and uraninite grains under different environmental and transport conditions (Fig. 6). The minimum O₂ levels to cause pyrite and uraninite destruction thus become maximum oxygen concentrations for these detrital grains to be preserved, and these values constrain the O₂ levels of Archean and early Paleoproterozoic Earth surface environments.

Due to differences in their oxidative weathering kinetics, the erosion rates of pyrite and uraninite—and consequently the maximum O₂ constraints generated from their

preservation in sedimentary successions—have different sensitivities to O_2 under various physical transport scenarios. These calculations predict that in modern short-transport systems, one might find detrital pyrite and uraninite present if they began as very large grains and if both were present in the source protolith (Fig. 8A). This prediction is consistent with our modern observations: we only occasionally find detrital pyrite and uraninite, in areas with rapid erosion and transport or high aridity (Holland, 1984). Indeed, pyrite and uraninite are known from some high-gradient alpine streams (Simpson and Bowles, 1977, 1981; Maynard et al., 1991). Yet this pyrite is being actively oxidatively weathered during transport in our current atmosphere and these grains do not survive into terminal deposits. Clearly by the end of even short rivers, even the largest initial pyrite and uraninite grains do not survive (Fig. 8A).

Our model is, however, limited by the accuracy of the chemical rate laws. Ono (2001) examined the Grandstaff chemical erosion relationship and found that some of the parameters, such as the factored dependence on oxygen, proton, and bicarbonate concentrations and his use of a geometric surface area in his calculations, may not be accurate or under certain conditions appropriate (Ono, 2001). This highlights the value of further experimental studies examining the controls on the oxidation of natural uraninite by O_2 . Nevertheless, the ability to observe the weathering behavior of these two different minerals in systems—particularly with independent information from observations of the sedimentary geology about transport processes, distances, and provenance (such as in Hofmann et al., 2009)—provides more precise O_2 constraints. An understanding of the

ancient basin geology and process sedimentology can indicate the paleo-river parameters, enabling a determination of river length and initial grain size. Knowing these river specifications, our model framework facilitates an understanding of ancient O₂ levels at the time of fluvial or marine deposition. These predictions can be applied in the context of Archean or Paleoproterozoic river systems, where the presence of redox-sensitive detrital grains in deposits provides an estimate of maximal O₂ in the atmosphere, or for later post-rise of oxygen successions from which the absence of these grains provides a lower bound on O₂ concentrations. For example, observing detrital pyrite grains in short-traveled conglomerates provides a less strict constraint on ancient O₂ levels. For the most part, these active systems are less likely to be preserved in the geological record over long timescales. Locally-sourced fluvial deposits associated with small isolated basins (ca. 100km²) during early phases of rifting, or glacial deposits (e.g., Williford et al., 2011) with a limited amount of transport and without any knowledge of the initial grain size, would be examples of systems with short travel distances. The presence of pyrite grains in these rapid transport systems does not constrain the O₂ to any lower than today, while the discovery of uraninite in these systems does constrain paleo-oxygen levels to at most 0.01 atm (Fig. 8A).

Redox-sensitive detrital grains observed in sedimentary rocks deposited at the termini of larger riverine systems—including the detrital pyrite and uraninite in the 2.415 Ga Koegas Subgroup deltaic deposits described here—constrain the O₂ concentrations to a much better extent because they offer a greater window of time for chemical erosion to

manifest even at exceedingly low O₂ concentrations. In the 100,000 to 500,000 year time span of large ancient rivers similar to the Amazon lowland and Ganges rivers (Granet et al., 2007; Dosseto et al., 2008), pyrite and uraninite both constrain the maximum O₂ levels to be 1×10^{-4} and 3.2×10^{-5} atm, respectively (Fig. 8B). A constraint of 3.2×10^{-5} atm effectively means environmental fluids in contact with these pyrite and uraninite grains had dissolved oxygen concentrations less than ~40 nM—perhaps substantially less. These are upper estimates, made purposefully conservative. In addition to modeling physical and chemical erosion processes separately rather than (more realistically) coupled, we have also only considered the chemical erosion of pyrite and uraninite by O₂ from abiotic oxidation rates and defect-free grains. This approach provides very conservative estimates for O₂, as much faster kinetics are expected by biological oxidation processes (e.g. Konhauser et al., 2011) and naturally-occurring pyrite and uraninite (Anbar et al., 2007; Reinhard et al., 2009).

The O₂ constraints from redox-sensitive detrital grains can be used to reflect on the interpretations made from other redox proxies. Though the nature and origin of mass anomalous sulfur isotope fractionations are not well-understood, our results support estimates from photochemical models that suggest this isotopic proxy is sensitive to very low O₂ levels (Pavlov and Kasting, 2002; Zahnle et al., 2006; Zerkle et al., 2012). In addition, widespread observations of redox-sensitive detrital grains provide an integrated first-order view of the lack of oxidative weathering processes across a range of environments on early Earth—from hillslopes to river channels, floodplains, and

nearshore marine environments. Though in our model framework some amounts of chemical erosion of grains can be permitted under certain transport scenarios (i.e., large initial size and low transport distance; Fig. 8), it is intriguing to wonder how much oxidative surface weathering did indeed occur during Archean and early Proterozoic time. A number of authors have proposed substantial amounts of pyrite weathering, yet the presence of well-preserved and rounded detrital pyrite grains throughout this interval without evidence for chemical erosion conflicts with these hypotheses (Anbar et al., 2007; Kaufman et al., 2007; Reinhard et al., 2009). Lastly, our observations imply the rise of oxygen is younger than 2.415 Ga, and is consistent with a wide range of results from sulfur isotope studies of Kaapvaal Craton strata (Bekker et al., 2004; Guo et al., 2009; Ono et al. 2009a; 2009b; Johnson et al. 2013).

The chemical erosion rate laws of pyrite and uraninite (equations 1 and 2) are directly responsible for differences in their weathering behavior and paleo-O₂ estimates from our calculations (Fig. 8). Despite the potential uncertainty with current understanding of the uraninite chemical erosion rate law (Ono, 2001), it is reasonable to think that these mineral phases will behave differently during oxidative weathering as a function of environmental O₂ concentrations. This forms the logic for an approach to identify intervals in Earth history wherein the atmosphere contained intermediate O₂ concentrations (e.g., levels that destroy uraninite but preserve pyrite in short-traveled fluvial systems). Systematic studies of the behavior of redox-sensitive detrital grains in Proterozoic-age siliciclastic successions would be valuable to test ideas of intermediate

oxygen concentrations following the initial rise of oxygen. It is important to note, however, that our current database of deposits shows uraninite and pyrite disappearing at about the same time from Canada (Pienaar, 1963; Robinson and Spooner, 1982; Krogh et al., 1984; Prasad and Roscoe, 1996), Brazil (Figueiredo, 1989), and South Africa (Johnson et al., 2013). The O₂ sensitivity and binary nature of the secular distribution of redox-sensitive grains in siliciclastic deposits suggests that the initial rise of oxygen was very substantial and oxygen levels never again dropped low enough to allow significant amounts of transport and preservation of either of these grains in either short- or long-traveled Earth surface weathering systems.

ACKNOWLEDGEMENTS

We would like to thank Grayson Chadwick for assistance with derivations and programming, as well as Chi Ma for support on the E-probe and SEM, and we are grateful to Chris Reinhard, Joel Scheingross, and two anonymous reviewers for feedback on the manuscript. We thank the Caltech Summer Undergraduate Research Fellowships (SURF) program, which co-sponsored A.G. to work on this project. J.E.J. acknowledges support from the NSF Graduate Research Fellowship program and W.W.F. acknowledges funding from the David and Lucile Packard Foundation. M.P.L. acknowledges support from NSF grant OCE-1233685, and the donors of the America Chemical Society Petroleum Research Fund. We thank the Agouron Institute for support of the South African Drilling Project.

FIGURES AND TABLES

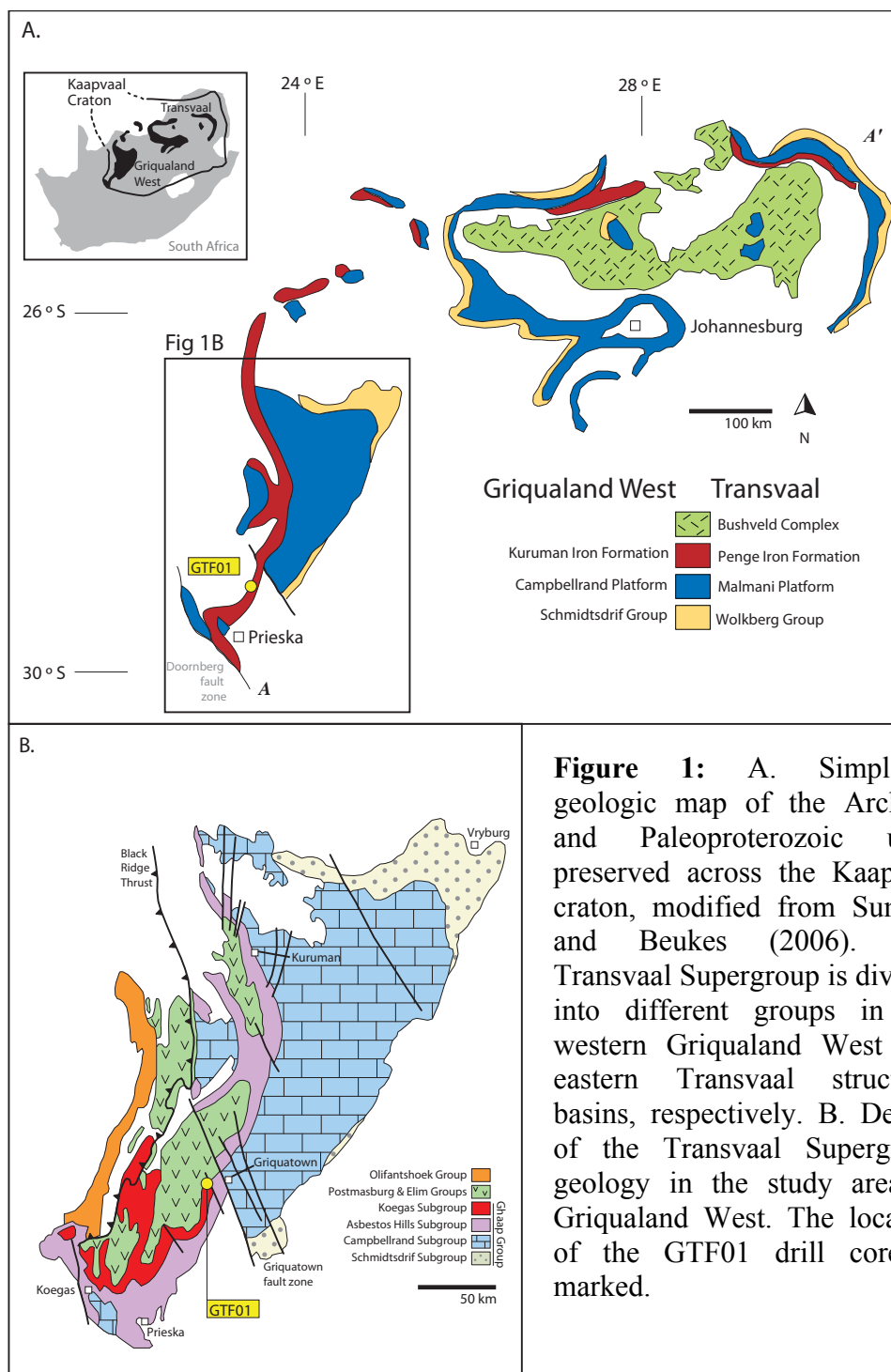


Figure 1: A. Simplified geologic map of the Archean and Paleoproterozoic units preserved across the Kaapvaal craton, modified from Sumner and Beukes (2006). The Transvaal Supergroup is divided into different groups in the western Griqualand West and eastern Transvaal structural basins, respectively. B. Details of the Transvaal Supergroup geology in the study area of Griqualand West. The location of the GTF01 drill core is marked.

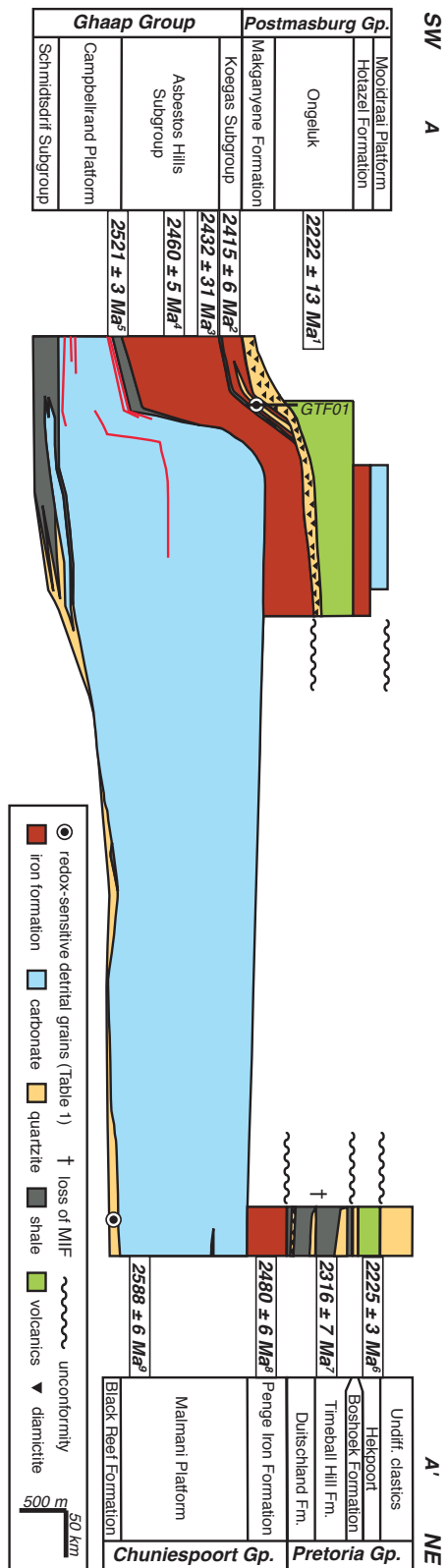


Figure 2: Stratigraphic cross section of the Transvaal Supergroup across the Kaapvaal craton from A to A' (see Fig. 1) based on stratigraphic data from Sumner and Beukes (2006). Key geochronologic constraints are shown from: 1. (Cornell et al., 1996) 2. (Gutzmer, Jens and Beukes, Nicolas, 1998) 3. (Trendall et al., 1990) 4. (Pickard, 2003) 5. (Sumner and Bowring, 1996) 6. (Yang and Holland, 2003) 7. (Hannah et al., 2004) 8. (Nelson et al., 1999) 9. (Martin et al., 1998). Also marked are redox constraints from mass-independent fractionation of sulfur isotopes (Bekker et al., 2004; Guo et al., 2009), detrital pyrite and uraninite (England et al., 2002; Hofmann et al., 2009; Johnson et al., 2013), and Mn deposits (Tsikos et al., 2003; Johnson et al., 2013).

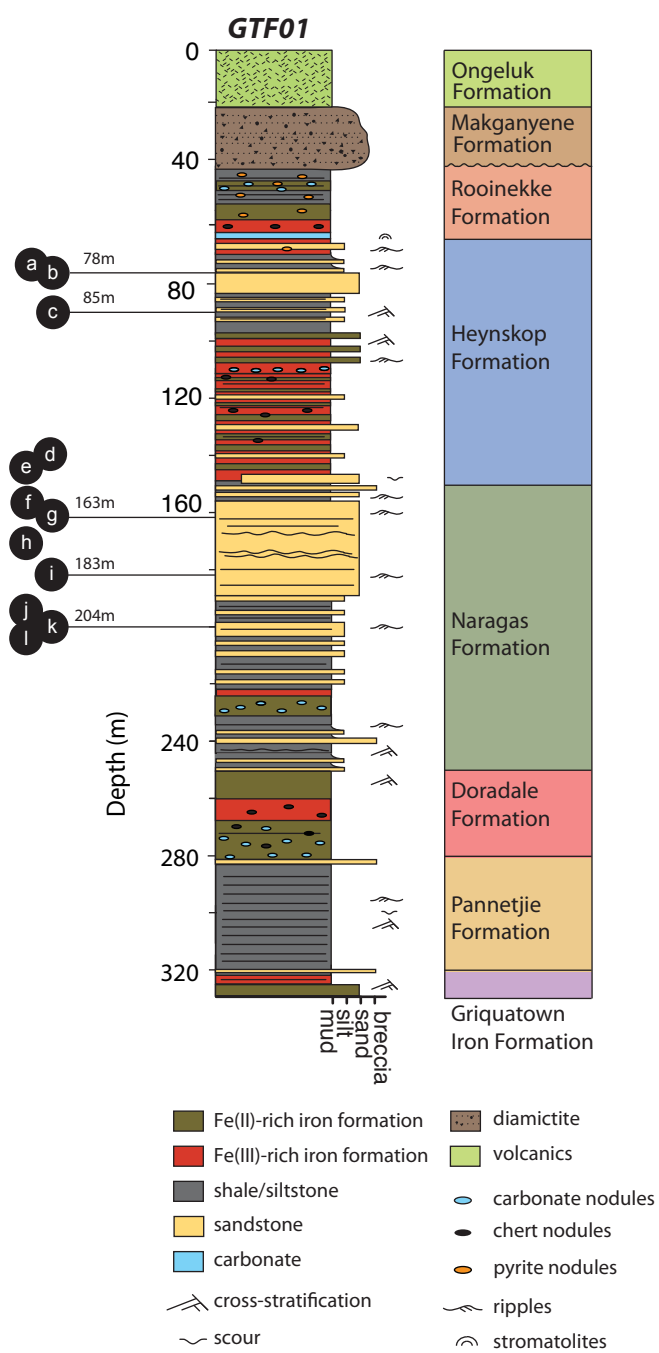


Figure 3: Stratigraphic section of GTF01 indicating formations and locations of redox-sensitive detrital grains photographed in Fig. 6.

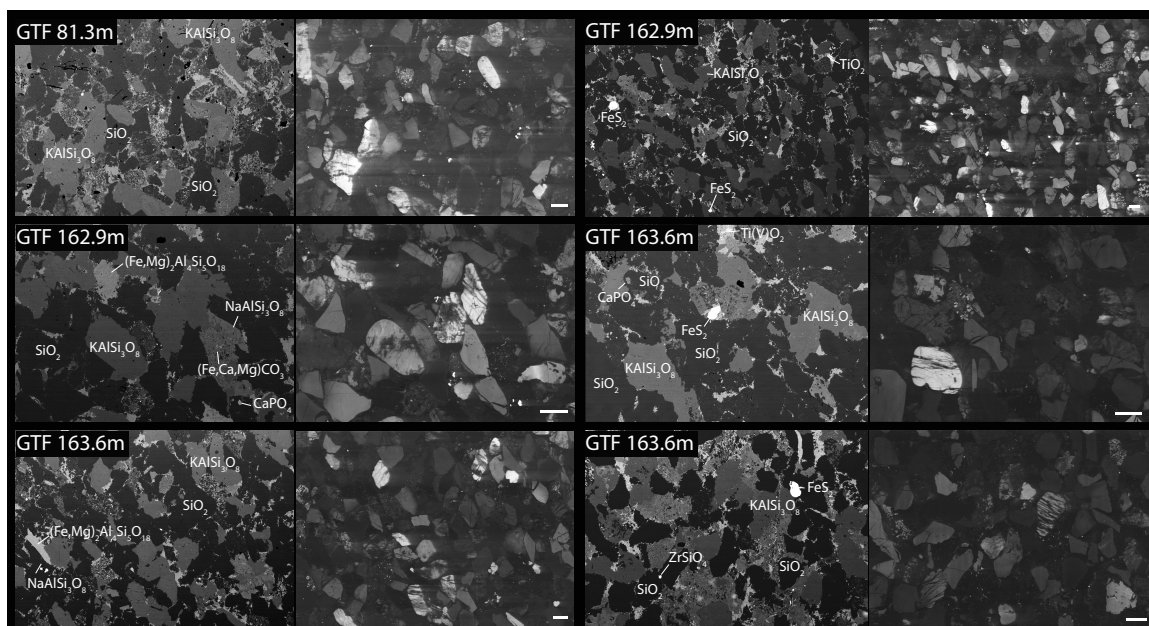


Figure 4: Sandstone textures from electron microscopy. Left panels show backscatter electron photomicrographs with detrital quartz, feldspar, and pyrite grains. Right panels depict the same view using variable pressure secondary electron images, highlighting via cathodoluminescence (CL) the rounding and truncation of quartz and feldspar zonation caused by physical abrasion. Scale bars are 100 μm .

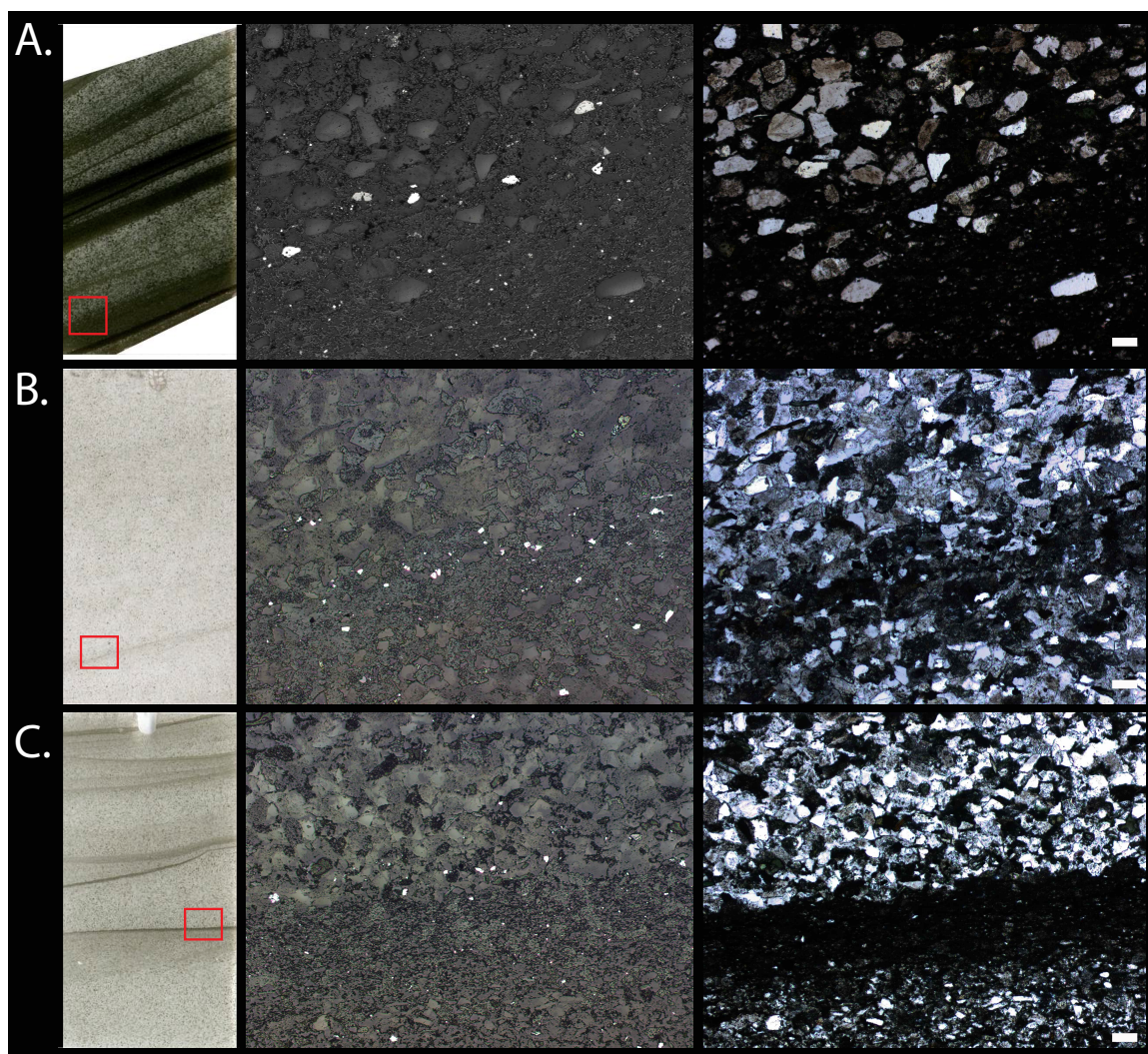


Figure 5: Pyrite distributions along ripple foreset laminae. A. GTF 78.75m, B. GTF 178.45m, C. GTF 182m, all showing (left to right) thin section image with target area marked in red, reflected light photograph of area indicating pyrite as bright white grains, and transmitted light photograph of same region. Scale bars are 100 μm .

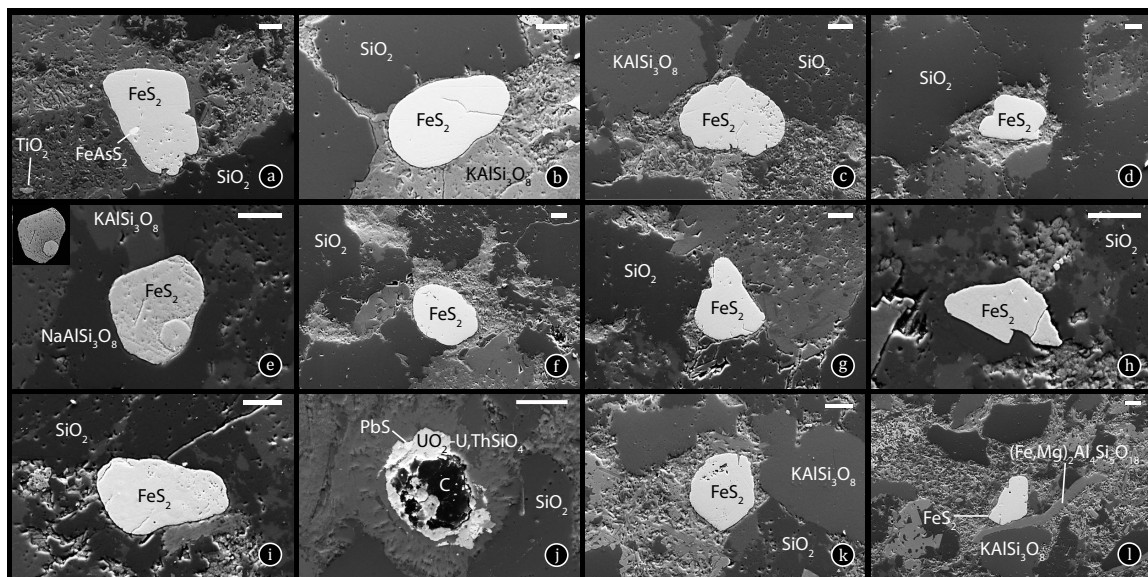
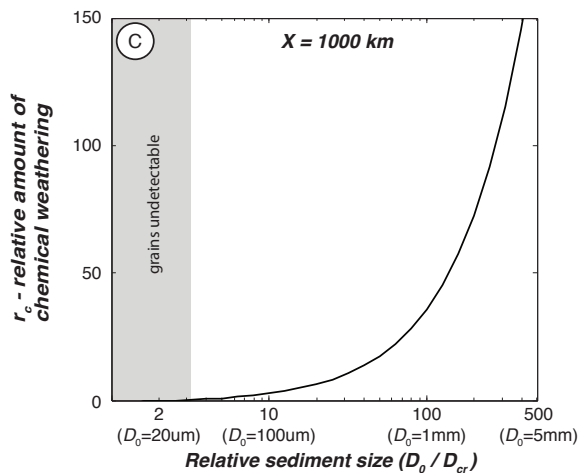
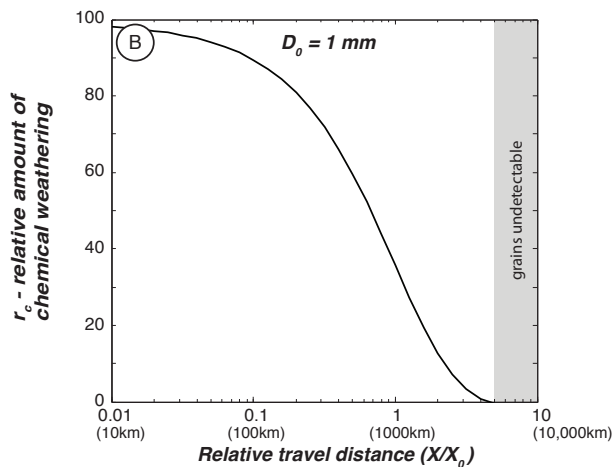
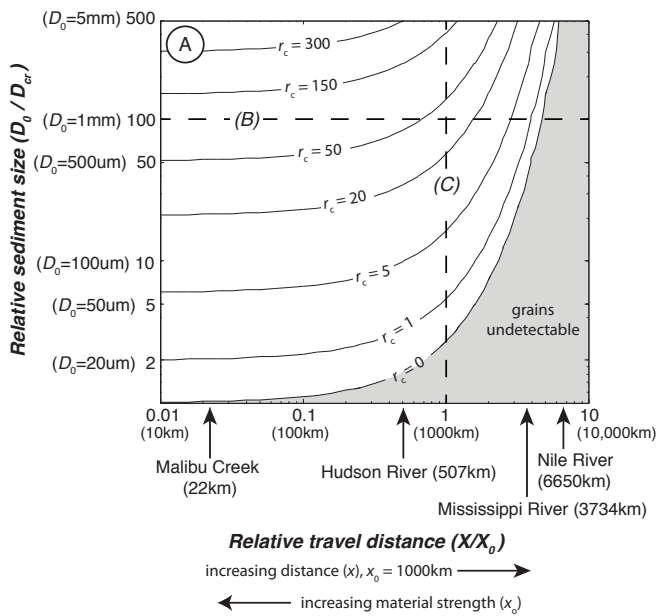


Figure 6: Backscatter electron photomicrographs showing examples of detrital pyrite and detrital uraninite found throughout thin sections of sandstones sampled from drill core. Letters correspond to specific stratigraphic samples shown in Fig. 3. Note inset of the pyrite grain in (e) with compositional differences and truncated internal zonation highlighted by high contrast. A detrital uraninite grain shown in (j) is now composed of uraninite-uranothorite with galena and bitumen inclusions due to radioactive decay (see text for details). Scale bars are 20 μm .

Figure 7 (below): A) Contours of the relative amount of chemical weathering (r_c) as a function of initial relative sediment diameter and relative grain travel distance for the parameter space realistic for Earth surface environments. Examples of initial sediment diameters (D_0) and river systems (with different lengths: x) are listed for comparison, assuming a critical sediment size for detection of $D_{cr} = 10 \mu\text{m}$ and an erodibility coefficient of $x_0 = 1000 \text{ km}$. Dashed lines marked “(B)” and “(C)” denote slices through solution space plotted in panels (B) and (C). B) Relative amount of chemical weathering (r_c) as a function of the relative distance traveled (x/x_0) of a grain with fixed relative initial size of $D_0 = 10 \mu\text{m}$. C) Relative amount of chemical weathering (r_c) as a function of relative initial sediment size (D_0/D_{cr}) for a fixed relative travel distance ($x = 1000 \text{ km}$). The shaded zones in all three panels are regions of parameter space where all grains are predicted to be smaller than the detection limit (i.e., $D < D_{cr}$).



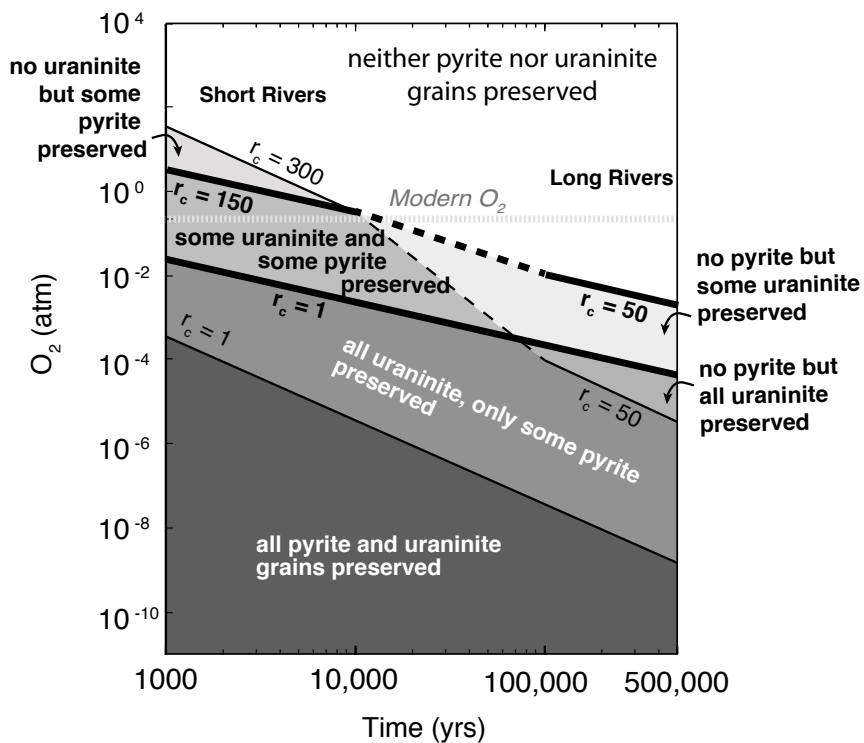
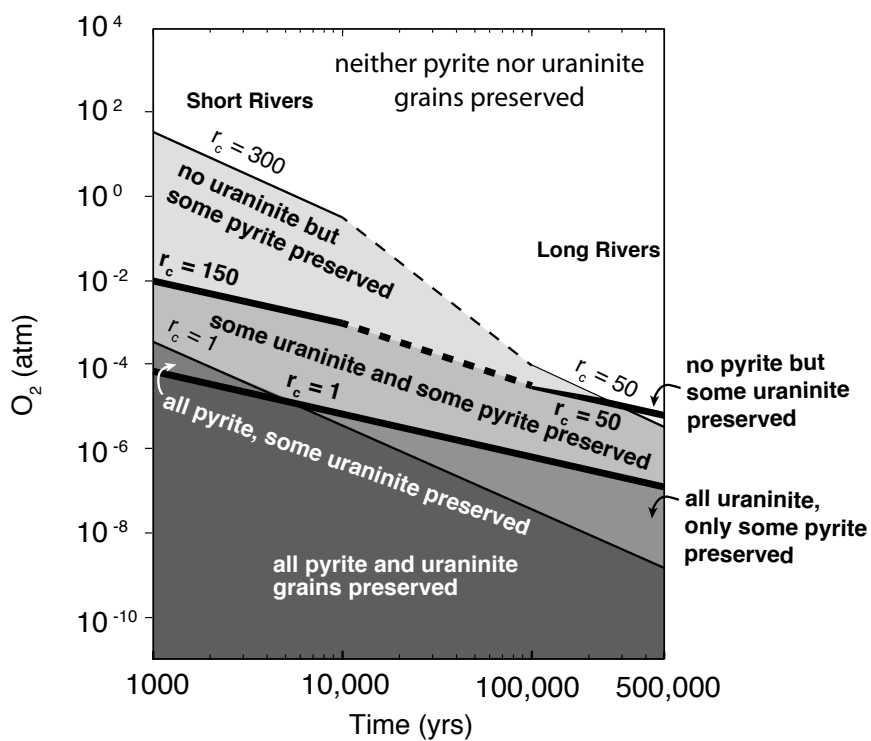
A. Modern conditions; $p\text{CO}_2 = 280$ ppmB. Archean and Paleoproterozoic conditions; $p\text{CO}_2 = 0.1$ atm

Figure 8: Upper bounds on environmental O₂ levels calculated for pyrite and uraninite preservation and destruction for the modern and Paleoproterozoic-Archean environment. The bounding values of relative chemical weathering in short river systems for pyrite ($1 < r_c < 300$; thin black lines) and uraninite ($1 < r_c < 150$; thick black lines) and long river systems for pyrite ($1 < r_c < 50$; thin black lines) and uraninite ($1 < r_c < 50$; thick black lines) come from the full range of environmental conditions explored in Figure 7A (see text for discussion), which incorporate a wide range of reasonable physical grain erosion rates and initial grain sizes. Dashed lines between the upper r_c estimates represent uncertainty as to when it is appropriate to change upper r_c bounds. Darkest grey area represents preservation of all pyrite and uraninite grains and white region represents no grain preservation, with intermediate shades of grey representing various scenarios of either pyrite or uraninite or both types of grains being only partially preserved. Labels for “Short Rivers” and “Long Rivers” from U-series disequilibria estimates (see text). A) Predicted levels of O₂ required for grain preservation and destruction as a function of transport time under modern (pre-industrial) CO₂ conditions. For modern O₂ levels (horizontal dotted line in pale grey), the model predicts preservation of pyrite and uraninite (shaded regions) over only relatively short timescales and relatively large r_c values, corresponding to environments with large protolith grain sizes and short transport distances. B) Calculated concentrations of O₂ for grain preservation and destruction as a function of transport time for a Paleoproterozoic or Archean environment with 0.1 atm of CO₂. Upper estimates on paleo-oxygen levels can be determined if reasonable knowledge of paleo-river distance and/or initial grain sizes are known.

TABLE 1. REPORTED OCCURRENCES OF REDOX-SENSITIVE DETRITAL GRAINS

Age (Ga)	Redox-sensitive grains	Rock environment and type	Stratigraphy	Reference
ca. 3.25	Pyrite, uraninite	Fluviodeltaic sandstones and conglomerates	Mosquito Creek Formation, Australia	Rasmussen and Buick (1999)
3.2–3.0	Pyrite, uraninite	Braided stream fluvial plain conglomerate	Bababudan Group, Dharwar Craton, South India	Srinivasan and Ojakangas (1986); Janardhan and Basavalingu (1988)
ca. 3.08	Pyrite, uraninite	Fluvial pebble conglomerate	Rhenosterspruit Formation, Dominion Group, South Africa	Hofmann et al. (2009); Simpson and Bowles (1977); Hiemstra (1968)
ca. 3–2.95	Pyrite, siderite	Fluvial sandstones	Lalla Rookh Formation, Australia	Rasmussen and Buick (1999)
ca. 2.95	Pyrite	Sandstone, wackestone, diamictite	Coronation Formation, West Rand Group, South Africa	Guy et al. (2010)
ca. 2.95	Pyrite, uraninite?*	Fluvial conglomerate to shallow marine sandstone	Mozaan Contact Reef, Mozaan Group, Pongola Supergroup, South Africa	Hofmann et al. (2009); Orberger et al. (2011); Hegner et al. (1994)
ca. 2.85	Pyrite, uraninite	Fluviodeltaic sandstones and conglomerates	Kimberley Reef, Central Rand Group, Witwatersrand Supergroup, South Africa	Kositcin and Krapez (2004); England et al. (2002); Hofmann et al. (2009)
2.77–2.715	Pyrite, uraninite, siderite	Braided river mature sandstones	Fortescue Group, Australia	Rasmussen and Buick (1999)
ca. 2.72	Pyrite, uraninite	Fluvial conglomerates interbedded with sandstones	Ventersport Formation, Ventersdorp Supergroup, South Africa	Krapez (1985); Hofmann et al. (2009)
ca. 2.64	Pyrite, uraninite	Fluvial fine-grained quartz and pebble conglomerate	Black Reef Quartzite Formation, South Africa	Barton and Hallbauer (1996); England et al. (2002); Walraven and Martini (1995); Gauert et al. (2011)
ca. 2.6	Pyrite	Marine turbidity current conglomerate, sandstone, shale deposits	Cheshire Formation, Belingwe greenstone belt, Zimbabwe	Hofmann et al. (2001, 2009)
2.58–2.42	Pyrite, uraninite	Fluvial conglomerates and coarse sandstones	Moeda Formation, Quadrilatero Ferrifero, Brazil	Villaca and Moura (1981); Minter et al. (1990); Hartmann et al. (2006)
2.66–2.1	Pyrite, uraninite	Fluviodeltaic conglomerates, sandstones, shales	Jacobina Group, Brazil	Figueiredo (1989)
ca. 2.45 (constrained 2.45–2.1 Ga)	Pyrite, uraninite	Conglomerates and sandstones, prograding alluvial fan(?) + deltaic deposits + fluvial cross-bedded quartz-pebble conglomerates	Rock Mountain Conglomerate, Bow Quartzite, Jack Hills Quartzite, Bridger Peak Quartzite, Sierra Madre and Medicine Bow Mountains, USA	Houston et al. (1992); Bekker et al. (2003)
2.45–2.22	Pyrite, uraninite	Fluviodeltaic conglomerates and sandstones	Matinenda Formation, Elliot Lake Group, Canada	Pienaar (1963); Robinson and Spooner (1982); Krogh et al. (1984); Prasad and Roscoe (1996)
ca. 2.415	Pyrite, uraninite	Deltaic sandstones	Naragas and Heynskop Formations, Koegas Subgroup, South Africa	Johnson et al. (2013); this study
2.42–2.22	Pyrite	Diamictite	Meteorite Bore Member, Kungarra Formation, Australia	Williford et al. (2011)

Note: Compiled from a variety of sources (see column 5). Approximate ages, redox-sensitive mineralogy, paleoenvironment and lithology, and stratigraphy from relevant reference are highlighted.
*Questionable due to poor preservation.

Table 1: Reported occurrences of redox-sensitive detrital grains.

Sample	% pyrite	% zircon	% apatite + monazite	% zircon + apatite + monazite
GTF 77.53m	0.4091	0.0055	0.2297	0.2352
GTF 163.65m	0.0398	0.0055	0.17	0.1755
GTF 203.65m	0.2638	0.0083	0.2688	0.2771
GTF 243.00m	0.1341	0.00075	0.2236	0.22435

Table 2: Abundances of detrital grains by mineralogy. Estimated using elemental abundance maps of S, Zr, and P as proxies for pyrite, zircon, and apatite+monazite from four representative sections. Note abundance of pyrite scales with abundance of combined heavy minerals (% zircon+apatite+monazite).

REFERENCES

- Anbar, A.D., Duan, Y., Lyons, T.W., Arnold, G.L., Kendall, B., Creaser, R.A., Kaufman, A.J., Gordon, G.W., Scott, C., Garvin, J., and Buick, R., 2007, A Whiff of Oxygen Before the Great Oxidation Event?: *Science*, v. 317, p. 1903–1906, doi: 10.1126/science.1140325.
- Barton, E.S., and Hallbauer, D.K., 1996, Trace-element and U-Pb isotope compositions of pyrite types in the Proterozoic Black Reef, Transvaal Sequence, South Africa: Implications on genesis and age: *Chemical Geology*, v. 133, p. 173–199, doi: 10.1016/S0009-2541(96)00075-7.
- Bekker, A., Holland, H.D., Wang, P.-L., Rumble, D., Stein, H.J., Hannah, J.L., Coetzee, L.L., and Beukes, N.J., 2004, Dating the rise of atmospheric oxygen: *Nature*, v. 427, p. 117–120, doi: 10.1038/nature02260.
- Bekker, A., Sial, A.N., Karhu, J.A., Ferreira, V.P., Noce, C.M., Kaufman, A.J., Romano, A.W., and Pimentel, M.M., 2003, Chemostratigraphy of Carbonates from the Minas Supergroup, Quadrilátero Ferrífero (Iron Quadrangle), Brazil: A Stratigraphic Record of Early Proterozoic Atmospheric, Biogeochemical and Climatic Change: *American Journal of Science*, v. 303, p. 865–904, doi: 10.2475/ajs.303.10.865.
- Beukes, N.J., 1987, Facies relations, depositional environments and diagenesis in a major early Proterozoic stromatolitic carbonate platform to basinal sequence, Campbellrand Subgroup, Transvaal Supergroup, Southern Africa: *Sedimentary Geology*, v. 54, p. 1–46, doi: 10.1016/0037-0738(87)90002-9.
- Beukes, N.J., Dorland, H., Gutzmer, J., Nedachi, M., and Ohmoto, H., 2002, Tropical laterites, life on land, and the history of atmospheric oxygen in the Paleoproterozoic: *Geology*, v. 30, p. 491–494, doi: 10.1130/0091-7613(2002)030<0491:TLLOLA>2.0.CO;2.
- Beukes, N.J., and Gutzmer, J., 2008, Origin and Paleoenvironmental Significance of Major Iron Formations at the Archean-Paleoproterozoic Boundary, *in* Hagemann, S., Rosiere, C., Gutzmer, J., and Beukes, N. eds., *Banded Iron Formation-Related High-Grade Ore*, p. 5–47.
- Beukes, N., and Klein, C., 1992, Models for Iron-Formation Deposition, *in* Schopf, J.W. and Klein, C. eds., *The Proterozoic Biosphere: A Multidisciplinary Study*, Cambridge University Press.
- Boggs, S., 2006, *Principles of sedimentology and stratigraphy*: Pearson Prentice Hall, 696 p.

- Le Bouteiller, C., Naaim-Bouvet, F., Mathys, N., and Lavé, J., 2011, A new framework for modeling sediment fining during transport with fragmentation and abrasion: *Journal of Geophysical Research: Earth Surface*, v. 116, p. n/a–n/a, doi: 10.1029/2010JF001926.
- Bradley, D.N., and Tucker, G.E., 2013, The storage time, age, and erosion hazard of laterally accreted sediment on the floodplain of a simulated meandering river: *Journal of Geophysical Research: Earth Surface*, v. 118, p. 1308–1319, doi: 10.1002/jgrf.20083.
- Cameron, E.M., 1982, Sulphate and sulphate reduction in early Precambrian oceans: *Nature*, v. 296, p. 145–148, doi: 10.1038/296145a0.
- Chabaux, F., Riotte, J., and Dequincey, O., 2003, U-Th-Ra Fractionation During Weathering and River Transport: *Reviews in Mineralogy and Geochemistry*, v. 52, p. 533–576, doi: 10.2113/0520533.
- Clemmey, H., and Badham, N., 1982, Oxygen in the Precambrian atmosphere: An evaluation of the geological evidence: *Geology*, v. 10, p. 141–146, doi: 10.1130/0091-7613(1982)10<141:OITPAA>2.0.CO;2.
- Cloud, P., 1972, A working model of the primitive Earth: *American Journal of Science*, v. 272, p. 537–548, doi: 10.2475/ajs.272.6.537.
- Cloud, P.E., 1968, Atmospheric and Hydrospheric Evolution on the Primitive Earth Both secular accretion and biological and geochemical processes have affected earth's volatile envelope: *Science*, v. 160, p. 729–736, doi: 10.1126/science.160.3829.729.
- Cornell, D.H., Schütte, S.S., and Eglington, B.L., 1996, The Ongeluk basaltic andesite formation in Griqualand West, South Africa: submarine alteration in a 2222 Ma proterozoic sea: *Precambrian Research*, v. 79, p. 101–123, doi: 10.1016/0301-9268(95)00090-9.
- DePaolo, D.J., Maher, K., Christensen, J.N., and McManus, J., 2006, Sediment transport time measured with U-series isotopes: Results from ODP North Atlantic drift site 984: *Earth and Planetary Science Letters*, v. 248, p. 394–410, doi: 10.1016/j.epsl.2006.06.004.
- Dosseto, A., Bourdon, B., Gaillardet, J., Allègre, C.J., and Filizola, N., 2006, Time scale and conditions of weathering under tropical climate: Study of the Amazon basin with U-series: *Geochimica et Cosmochimica Acta*, v. 70, p. 71–89, doi: 10.1016/j.gca.2005.06.033.

- Dosseto, A., Bourdon, B., and Turner, S.P., 2008, Uranium-series isotopes in river materials: Insights into the timescales of erosion and sediment transport: *Earth and Planetary Science Letters*, v. 265, p. 1–17, doi: 10.1016/j.epsl.2007.10.023.
- England, G.L., Rasmussen, B., Krapež, B., and Groves, D.I., 2002, Palaeoenvironmental significance of rounded pyrite in siliciclastic sequences of the Late Archaean Witwatersrand Basin: oxygen-deficient atmosphere or hydrothermal alteration?: *Sedimentology*, v. 49, p. 1133–1156, doi: 10.1046/j.1365-3091.2002.00479.x.
- England, G.L., Rasmussen, B., Krapež, B., and Groves, D.I., 2001, The Origin of Uraninite, Bitumen Nodules, and Carbon Seams in Witwatersrand Gold-Uranium-Pyrite Ore Deposits, Based on a Permo-Triassic Analogue: *Economic Geology*, v. 96, p. 1907–1920, doi: 10.2113/gsecongeo.96.8.1907.
- Ferrier, K.L., and Kirchner, J.W., 2008, Effects of physical erosion on chemical denudation rates: A numerical modeling study of soil-mantled hillslopes: *Earth and Planetary Science Letters*, v. 272, p. 591–599, doi: 10.1016/j.epsl.2008.05.024.
- Figueiredo, M.C.H., 1989, Geochemical evolution of eastern Bahia, Brazil: A probable Early Proterozoic subduction-related magmatic arc: *Journal of South American Earth Sciences*, v. 2, p. 131–145, doi: 10.1016/0895-9811(89)90041-2.
- Finch, R., and Murakami, T., 1999, Systematics and paragenesis of uranium minerals: *Reviews in Mineralogy and Geochemistry*, v. 38, p. 91–179.
- Folk, R.L., 1957, *Petrology of Sedimentary Rocks*: Austin, Texas: University of Texas.
- Gauert, C.D.K., Brauns, M., Batchelor, D., and Simon, R., 2011, Gold Provenance of the Black Reef Conglomerate, West and East Rand, South Africa, *in* SGA Abs. Volumes,.
- Grandstaff, D.E., 1976, A kinetic study of the dissolution of uraninite: *Economic Geology*, v. 71, p. 1493–1506, doi: 10.2113/gsecongeo.71.8.1493.
- Grandstaff, D.E., 1980, Origin of uraniferous conglomerates at Elliot Lake, Canada and Witwatersrand, South Africa - Implications for oxygen in the Precambrian atmosphere: *Precambrian Research*, v. 13, p. 1–26.
- Granet, M., Chabaux, F., Stille, P., Dosseto, A., France-Lanord, C., and Blaes, E., 2010, U-series disequilibria in suspended river sediments and implication for sediment transfer time in alluvial plains: The case of the Himalayan rivers: *Geochimica et Cosmochimica Acta*, v. 74, p. 2851–2865, doi: 10.1016/j.gca.2010.02.016.

- Granet, M., Chabaux, F., Stille, P., France-Lanord, C., and Pelt, E., 2007, Time-scales of sedimentary transfer and weathering processes from U-series nuclides: Clues from the Himalayan rivers: *Earth and Planetary Science Letters*, v. 261, p. 389–406, doi: 10.1016/j.epsl.2007.07.012.
- Grotzinger, J.P., and Kasting, J.F., 1993, New constraints on Precambrian ocean composition: *The Journal of geology*, v. 101, p. 235–243.
- Guo, Q., Strauss, H., Kaufman, A.J., Schröder, S., Gutzmer, J., Wing, B., Baker, M.A., Bekker, A., Jin, Q., Kim, S.-T., and Farquhar, J., 2009, Reconstructing Earth's Surface Oxidation Across the Archean-Proterozoic Transition: *Geology*, v. 37, p. 399–402, doi: 10.1130/G25423A.1.
- Gutzmer, Jens, and Beukes, Nicolas, 1998, High-grade manganese ores in the Kalahari manganese field: characterisation and dating of ore forming events: Rand Afrikaans University Unpublished Report, 221 p.
- Guy, B.M., Beukes, N.J., and Gutzmer, J., 2010, Paleoenvironmental Controls on the Texture and Chemical Composition of Pyrite from Non-Conglomeratic Sedimentary Rocks of the Mesoproterozoic Witwatersrand Supergroup, South Africa: *South African Journal of Geology*, v. 113, p. 195–228, doi: 10.2113/gssajg.113.2.195.
- Halevy, I., Pierrehumbert, R.T., and Schrag, D.P., 2009, Radiative transfer in CO₂-rich paleoatmospheres: *Journal of Geophysical Research (Atmospheres)*, v. 114, p. 18112, doi: 10.1029/2009JD011915.
- Hallbauer, D.K., and Utter, T., 1977, Geochemical and morphological characteristics of gold particles from recent river deposits and the fossil placers of the Witwatersrand: *Mineralium Deposita*, v. 12, p. 293–306.
- Handley, H.K., Turner, S., Afonso, J.C., Dosseto, A., and Cohen, T., 2013, Sediment residence times constrained by uranium-series isotopes: A critical appraisal of the comminution approach: *Geochimica et Cosmochimica Acta*, v. 103, p. 245–262, doi: 10.1016/j.gca.2012.10.047.
- Hannah, J.L., Bekker, A., Stein, H.J., Markey, R.J., and Holland, H.D., 2004, Primitive Os and 2316 Ma age for marine shale: implications for Paleoproterozoic glacial events and the rise of atmospheric oxygen: *Earth and Planetary Science Letters*, v. 225, p. 43–52, doi: 10.1016/j.epsl.2004.06.013.
- Hartmann, L.A., Endo, I., Suita, M.T.F., Santos, J.O.S., Frantz, J.C., Carneiro, M.A., McNaughton, N.J., and Barley, M.E., 2006, Provenance and age delimitation of Quadrilátero Ferrífero sandstones based on zircon U–Pb isotopes: *Journal of*

South American Earth Sciences, v. 20, p. 273–285, doi:
10.1016/j.jsames.2005.07.015.

Hegner, E., Kröner, A., and Hunt, P., 1994, A precise U-Pb zircon age for the Archaean Pongola Supergroup volcanics in Swaziland: *Journal of African Earth Sciences*, v. 18, p. 339–341, doi: 10.1016/0899-5362(94)90072-8.

Hiemstra, S.A., 1968, The mineralogy and petrology of the uraniferous conglomerate of the Dominion Reefs Mine, Klerksdorp area: *Trans. Geol. Soc. S. Afr.*, v. 71, p. 1–65.

Hofmann, A., Bekker, A., Rouxel, O., Rumble, D., and Master, S., 2009, Multiple sulphur and iron isotope composition of detrital pyrite in Archaean sedimentary rocks: A new tool for provenance analysis: *Earth and Planetary Science Letters*, v. 286, p. 436–445, doi: 10.1016/j.epsl.2009.07.008.

Hofmann, A., Dirks, P.H.G., and Jelsma, H., 2001, Late Archaean foreland basin deposits, Belingwe greenstone belt, Zimbabwe: *Sedimentary Geology*, v. 141–142, p. 131–168, doi: 10.1016/S0037-0738(01)00072-0.

Holland, H.D., 1984, *The Chemical Evolution of the Atmosphere and Oceans*: Princeton University Press, 598 p.

Houston, R.S., Karlstrom, K.E., Graff, P.J., and Flurkey, A.J., 1992, New Stratigraphic Subdivisions and Redefinition of Subdivisions of Late Archean and Early Proterozoic Metasedimentary and Metavolcanic Rocks of the Sierra Madre and Medicine Bow Mountains, Southern Wyoming: U.S. Geological Survey Professional Paper, v. 1520, p. 1–50.

Janardhan, A.S.F., and Basavalingu, B., 1988, Sedimentology, Mineralogy and Geochemistry of the Kalasapura Conglomerate: *Memoir Geological Society of India*, v. 9, p. 65–82.

Janeczek, J., and Ewing, R.C., 1992, Dissolution and alteration of uraninite under reducing conditions: *Journal of Nuclear Materials*, v. 190, p. 157–173, doi: 10.1016/0022-3115(92)90084-X.

Johnson, J.E., Webb, S.M., Thomas, K., Ono, S., Kirschvink, J.L., and Fischer, W.W., 2013, Manganese-oxidizing photosynthesis before the rise of cyanobacteria: *PNAS*, in press.

Joseph, G.G., and Hunt, M.L., 2004, Oblique particle-wall collisions in a liquid: *J. Fluid Mech.*, v. 510, p. 71–93.

- Kaufman, A.J., Johnston, D.T., Farquhar, J., Masterson, A.L., Lyons, T.W., Bates, S., Anbar, A.D., Arnold, G.L., Garvin, J., and Buick, R., 2007, Late Archean Biospheric Oxygenation and Atmospheric Evolution: *Science*, v. 317, p. 1900–1903, doi: 10.1126/science.1138700.
- Kodama, Y., 1994, Experimental study of abrasion and its role in producing downstream fining in gravel-bed rivers: *Journal of Sedimentary Research*, v. 64, p. 76–85.
- Kong, M., Bhattacharya, R.N., James, C., and Basu, A., 2005, A statistical approach to estimate the 3D size distribution of spheres from 2D size distributions: *Geological Society of America Bulletin*, v. 117, p. 244–249, doi: 10.1130/B25000.1.
- Konhauser, K.O., Lalonde, S.V., Planavsky, N.J., Pecoits, E., Lyons, T.W., Mojzsis, S.J., Rouxel, O.J., Barley, M.E., Rosiere, C., Fralick, P.W., Kump, L.R., and Bekker, A., 2011, Aerobic bacterial pyrite oxidation and acid rock drainage during the Great Oxidation Event: *Nature*, v. 478, p. 369–373, doi: 10.1038/nature10511.
- Kositcin, N., and Krapez, B., 2004, Relationship between detrital zircon age-spectra and the tectonic evolution of the Late Archaean Witwatersrand Basin, South Africa: *Precambrian Research*, v. 129, p. 141–168.
- Kozhevnikov, V., Skublov, S., Marin, Y., Medvedev, P., Systra, Y., and Valencia, V., 2010, Hadean-archean detrital zircons from Jatulian quartzites and conglomerates of the Karelian craton: *Doklady Earth Sciences*, v. 431, p. 318–323, doi: 10.1134/S1028334X10030128.
- Krapez, B., 1985, The Ventersdorp Contact placer: a gold-pyrite placer of stream and debris-flow origins from the Archaean Witwatersrand Basin of South Africa: *Sedimentology*, v. 32, p. 223–234, doi: 10.1111/j.1365-3091.1985.tb00505.x.
- Krogh, T.E., Davis, D.W., and Corfu, F., 1984, Precise U-Pb zircon and baddeleyite ages for the Sudbury area, *in* The geology and ore deposits of the Sudbury Structure, Ontario, Geological Survey Special Volume 1, Energy, Mines and Resources Canada, p. 431–446.
- Lamb, M.P., Dietrich, W.E., and Sklar, L.S., 2008, A model for fluvial bedrock incision by impacting suspended and bed load sediment: *Journal of Geophysical Research: Earth Surface*, v. 113, p. n/a–n/a, doi: 10.1029/2007JF000915.
- Lauer, J.W., and Parker, G., 2008, Modeling framework for sediment deposition, storage, and evacuation in the floodplain of a meandering river: *Theory: Water Resources Research*, v. 44, p. n/a–n/a, doi: 10.1029/2006WR005528.

- Lee, V.E., DePaolo, D.J., and Christensen, J.N., 2010, Uranium-series comminution ages of continental sediments: Case study of a Pleistocene alluvial fan: *Earth and Planetary Science Letters*, v. 296, p. 244–254, doi: 10.1016/j.epsl.2010.05.005.
- Lewin, J., and Brewer, P.A., 2002, Laboratory simulation of clast abrasion: *Earth Surface Processes and Landforms*, v. 27, p. 145–164, doi: 10.1002/esp.306.
- Liebenberg, W.R., 1955, The Occurrence and Origin of Gold and Radioactive Minerals in the Witwatersrand System, the Dominion Reef, the Ventersdorp Contact Reef and the Black Reef: Geological Society of South Africa, 154 p.
- Martin, D.M., Clendenin, C.W., Krapez, B., and McNaughton, N.J., 1998, Tectonic and geochronological constraints on late Archaean and Palaeoproterozoic stratigraphic correlation within and between the Kaapvaal and Pilbara Cratons.: *Journal of the Geological Society of Australia*, v. 155, p. 311–322.
- Maynard, J.B., Ritger, S.D., and Sutton, S.J., 1991, Chemistry of sands from the modern Indus River and the Archean Witwatersrand basin: Implications for the composition of the Archean atmosphere: *Geology*, v. 19, p. 265–268, doi: 10.1130/0091-7613(1991)019<0265:CO&SFTM>2.3.CO;2.
- McDowell, J.P., 1957, The Sedimentary Petrology of the Mississagi Quartzite in the Blind River Area: Baptist Johnston, 31 p.
- Mikoš, M., 1995, Fluvial abrasion; converting size reduction coefficients into weight reduction rates: *Journal of Sedimentary Research*, v. 65, p. 472–476, doi: 10.1306/D42680FE-2B26-11D7-8648000102C1865D.
- Minter, W.E.L., Renger, F.E., and Siegers, A., 1990, Early Proterozoic gold placers of the Moeda Formation within the Gandarela Syncline, Minas Gerais, Brazil: *Economic Geology*, v. 85, p. 943–951, doi: 10.2113/gsecongeo.85.5.943.
- Nelson, D.R., Trendall, A.F., and Altermann, W., 1999, Chronological correlations between the Pilbara and Kaapvaal cratons: *Precambrian Research*, v. 97, p. 165–189, doi: 10.1016/S0301-9268(99)00031-5.
- Ono, S., 2001, Detrital uraninite and the early earth's atmosphere: SIMS analyses of uraninite in the Elliot Lake District and the dissolution kinetics of natural uraninite: Pennsylvania State University.
- Orberger, B., Hoffmann, A., Hicks, N., Wirth, R., Tudryn, A., and Megneng, M., 2011, Uranium mineralization in carbonaceous chert pebbles from Mesoarchean Mozaan Group conglomerates (~3 Ga, Pongola Basin, South Africa): trap or source rock?, in 11th SGA Biennial Meeting “Let's talk ore Deposits” Conference, Antofagasta, Chili.

- Papineau, D., Mojzsis, S.J., and Schmitt, A.K., 2007, Multiple sulfur isotopes from Paleoproterozoic Huronian interglacial sediments and the rise of atmospheric oxygen: *Earth and Planetary Science Letters*, v. 255, p. 188–212, doi: 10.1016/j.epsl.2006.12.015.
- Pavlov, A.A., and Kasting, J.F., 2002, Mass-Independent Fractionation of Sulfur Isotopes in Archean Sediments: Strong Evidence for an Anoxic Archean Atmosphere: *Astrobiology*, v. 2, p. 27–41, doi: 10.1089/153110702753621321.
- Pickard, A., 2003, SHRIMP U–Pb zircon ages for the Palaeoproterozoic Kuruman Iron Formation, Northern Cape Province, South Africa: evidence for simultaneous BIF deposition on Kaapvaal and Pilbara Cratons: *Precambrian Research*, v. 125, p. 275–315, doi: 10.1016/S0301-9268(03)00113-X.
- Pienaar, P.J., 1963, Stratigraphy, petrology, and genesis of the Elliot Group, Blind River, Ontario.: Including the uraniferous conglomerate.,: Dept. of Mines and Technical Surveys, Canada, 140 p.
- Prasad, N., and Roscoe, S.M., 1996, Evidence of anoxic to oxic atmospheric change during 2.45–2.22 Ga from lower and upper sub-Huronian paleosols, Canada: *CATENA*, v. 27, p. 105–121, doi: 10.1016/0341-8162(96)00003-3.
- Pufahl, P.K., and Hiatt, E.E., 2012, Oxygenation of the Earth's atmosphere–ocean system: A review of physical and chemical sedimentologic responses: *Marine and Petroleum Geology*, v. 32, p. 1–20, doi: 10.1016/j.marpetgeo.2011.12.002.
- Ramdohr, P., 1958, New observations on the ores of the Witwatersrand in South Africa and their genetic significance: *Geological Society of South Africa*, 186 p.
- Rasmussen, B., and Buick, R., 1999, Redox State of the Archean Atmosphere: Evidence from Detrital Heavy Minerals in Ca. 3250–2750 Ma Sandstones from the Pilbara Craton, Australia: *Geology*, v. 27, p. 115–118, doi: 10.1130/0091-7613(1999)027<0115:RSOTAA>2.3.CO;2.
- Reinhard, C.T., Raiswell, R., Scott, C., Anbar, A.D., and Lyons, T.W., 2009, A late Archean sulfidic sea stimulated by early oxidative weathering of the continents: *Science (New York, N.Y.)*, v. 326, p. 713–716, doi: 10.1126/science.1176711.
- Riebe, C.S., Kirchner, J.W., and Finkel, R.C., 2003, Long-term rates of chemical weathering and physical erosion from cosmogenic nuclides and geochemical mass balance: *Geochimica et Cosmochimica Acta*, v. 67, p. 4411–4427, doi: 10.1016/S0016-7037(03)00382-X.

- Robinson, A., and Spooner, E.T.C., 1982, Source of the detrital components of uraniferous conglomerates, Quirke ore zone, Elliot Lake, Ontario, Canada: *Nature*, v. 299, p. 622–624, doi: 10.1038/299622a0.
- Roscoe, S.M., 1973, The Huronian Supergroup, a Paleoproterozoic succession showing evidence of atmospheric evolution, *in* Young, G.M. ed., *Huronian Stratigraphy and Sedimentation*, Geological Association of Canada, p. 31–47.
- Rye, R., and Holland, H.D., 1998, Paleosols and the evolution of atmospheric oxygen: a critical review: *American journal of science*, v. 298, p. 621–672.
- Rye, R., Kuo, P.H., and Holland, H.D., 1995, Atmospheric carbon dioxide concentrations before 2.2 billion years ago: *Nature*, v. 378, p. 603–605, doi: 10.1038/378603a0.
- Schmeeckle, M.W., Nelson, J.M., Pitlick, J., and Bennett, J.P., 2001, Interparticle collision of natural sediment grains in water: *Water Resources Research*, v. 37, p. 2377–2391, doi: 10.1029/2001WR000531.
- Schmitz, M.D., and Bowring, S.A., 2003, Ultrahigh-temperature metamorphism in the lower crust during Neoproterozoic Ventersdorp rifting and magmatism, Kaapvaal Craton, southern Africa: *Geological Society of America Bulletin*, v. 115, p. 533–548, doi: 10.1130/0016-7606(2003)115<0533:UMITLC>2.0.CO;2.
- Schröder, S., Bedorf, D., Beukes, N.J., and Gutzmer, J., 2011, From BIF to red beds: Sedimentology and sequence stratigraphy of the Paleoproterozoic Koegas Subgroup (South Africa): *Sedimentary Geology*, v. 236, p. 25–44, doi: 10.1016/j.sedgeo.2010.11.007.
- Shaw, J., and Kellerhals, R., 1982, *The Composition of Recent Alluvial Gravels in Alberta River Beds*: Alberta Research Council Alberta Geological Survey, 151 p.
- Sheldon, N.D., 2006, Precambrian paleosols and atmospheric CO₂ levels: *Precambrian Research*, v. 147, p. 148–155, doi: 10.1016/j.precamres.2006.02.004.
- Simonson, B.M., and Hassler, S.W., 1996, Was the Deposition of Large Precambrian Iron Formations Linked to Major Marine Transgressions?: *Journal of Geology*, v. 104, p. 665–676, doi: 10.1086/629861.
- Simpson, P.R., and Bowles, J.F., 1981, *Detrital Uraninite and Pyrite: Are They Evidence for a Reducing Atmosphere?*: U.S. Geological Survey, book p.
- Simpson, P.R., and Bowles, J.F.W., 1977, Uranium Mineralization of the Witwatersrand and Dominion Reef Systems: *Philosophical Transactions of the Royal Society of London. Series A, Mathematical and Physical Sciences*, v. 286, p. 527–548, doi: 10.1098/rsta.1977.0130.

- Sklar, L.S., Dietrich, W.E., Foufoula-Georgiou, E., Lashermes, B., and Bellugi, D., 2006, Do gravel bed river size distributions record channel network structure?: *Water Resources Research*, v. 42.
- Srinivasan, R., and Ojakangas, R.W., 1986, Sedimentology of Quartz-Pebble Conglomerates and Quartzites of the Archean Bababudan Group, Dharwar Craton, South India: Evidence for Early Crustal Stability: *The Journal of Geology*, v. 94, p. 199–214, doi: 10.1086/629023.
- Sternberg, H., 1875, Untersuchungen uber Langen-und Querprofil geschiebefuhrender Flusse: *Zeitschrift fur Bauwesen*, v. XXV, p. 483–506.
- Stumm, W., and Morgan, J.J., 1996, *Aquatic Chemistry: Chemical Equilibria and Rates in Natural Waters*: Wiley-Interscience, 1040 p.
- Sumner, D.Y., and Beukes, N.J., 2006, Sequence stratigraphic development of the Neoproterozoic Transvaal carbonate platform, Kaapvaal Craton, South Africa: v. 109.
- Sumner, D.Y., and Bowring, S.A., 1996, U-Pb geochronologic constraints on deposition of the Campbellrand Subgroup, Transvaal Supergroup, South Africa: *Precambrian Research*, v. 79, p. 25–35, doi: 10.1016/0301-9268(95)00086-0.
- Tabakh, M.E., Grey, K., Pirajno, F., and Schreiber, B.C., 1999, Pseudomorphs after evaporitic minerals interbedded with 2.2 Ga stromatolites of the Yerrida basin, Western Australia: Origin and significance: *Geology*, v. 27, p. 871–874, doi: 10.1130/0091-7613(1999)027<0871:PAEMIW>2.3.CO;2.
- Trendall, A.F., Compston, W., Williams, I.S., Armstrong, R.A., Arndt, N.T., McNaughton, N.J., Nelson, D.R., Barley, M.E., Beukes, N.J., De Laeter, J.R., Retief, E.A., and Thorne, A.M., 1990, Precise zircon U–Pb chronological comparison of the volcano-sedimentary sequences of the Kaapvaal and Pilbara Cratons between about 3.1 and 2.4 Ga, *in* *Proceedings of the Third International Archaean Symposium*, Perth, Geological Society of Australia, p. 81–83.
- Tsikos, H., Beukes, N.J., Moore, J.M., and Harris, C., 2003, Deposition, Diagenesis, and Secondary Enrichment of Metals in the Paleoproterozoic Hotazel Iron Formation, Kalahari Manganese Field, South Africa: *Economic Geology*, v. 98, p. 1449–1462, doi: 10.2113/gsecongeo.98.7.1449.
- Utsunomiya, S., Murakami, T., Nakada, M., and Kasama, T., 2003, Iron oxidation state of a 2.45-Byr-old paleosol developed on mafic volcanics: *Geochimica et Cosmochimica Acta*, v. 67, p. 213–221, doi: 10.1016/S0016-7037(02)01083-9.

- Vigier, N., Bourdon, B., Turner, S., and Allègre, C.J., 2001, Erosion timescales derived from U-decay series measurements in rivers: *Earth and Planetary Science Letters*, v. 193, p. 549–563, doi: 10.1016/S0012-821X(01)00510-6.
- Vigier, N., Burton, K.W., Gislason, S.R., Rogers, N.W., Duchene, S., Thomas, L., Hodge, E., and Schaefer, B., 2006, The relationship between riverine U-series disequilibria and erosion rates in a basaltic terrain: *Earth and Planetary Science Letters*, v. 249, p. 258–273, doi: 10.1016/j.epsl.2006.07.001.
- Villaca, J.N., and Moura, L.A.M., 1981, Uranium in Precambrian Moeda Formation, Minas Gerais, Brazil, *in* *Genesis of Uranium- and Gold-Bearing Precambrian Quartz-Pebble Conglomerates*, Geological Survey Professional Paper, U.S. Government Printing Office.
- Walraven, F., and Martini, J., 1995, Zircon Pb-evaporation age determinations for the Oak Tree Formation, Chuniespoort Group, Transvaal Sequence; implications for Transvaal-Griqualand West basin correlations: *South African Journal of Geology*, v. 98, p. 58–67.
- Wentworth, C.K., 1922, A scale of grade and class terms for clastic sediments: *Journal of Geology*, v. 30, p. 377–392.
- Williamson, M.A., and Rimstidt, J.D., 1994, The kinetics and electrochemical rate-determining step of aqueous pyrite oxidation: *Geochimica et Cosmochimica Acta*, v. 58, p. 5443–5454, doi: 10.1016/0016-7037(94)90241-0.
- Williford, K.H., Van Kranendonk, M.J., Ushikubo, T., Kozdon, R., and Valley, J.W., 2011, Constraining atmospheric oxygen and seawater sulfate concentrations during Paleoproterozoic glaciation: In situ sulfur three-isotope microanalysis of pyrite from the Turee Creek Group, Western Australia: *Geochimica et Cosmochimica Acta*, v. 75, p. 5686–5705, doi: 10.1016/j.gca.2011.07.010.
- Yang, W., and Holland, H.D., 2003, The Hekpoort paleosol profile in Strata 1 at Gaborone, Botswana: Soil formation during the Great Oxidation Event: *American Journal of Science*, v. 303, p. 187–220, doi: 10.2475/ajs.303.3.187.
- Zahnle, K., Claire, M., and Catling, D., 2006, The loss of mass-independent fractionation in sulfur due to a Palaeoproterozoic collapse of atmospheric methane: *Geobiology*, v. 4, p. 271–283, doi: 10.1111/j.1472-4669.2006.00085.x.
- Zerle, A.L., Claire, M.W., Domagal-Goldman, S.D., Farquhar, J., and Poulton, S.W., 2012, A bistable organic-rich atmosphere on the Neoproterozoic Earth: *Nature Geoscience*, v. 5, p. 359–363, doi: 10.1038/ngeo1425.